

FACULDADE DE ENGENHARIA DA UNIVERSIDADE DO PORTO

# Optimized Meshing for Rocket Combustion Chambers Simulations

Henrique Alas Martins Cestaro



Mestrado em Mecânica Computacional

Supervisor at FEUP: Prof. Dr. José César de Sá

Supervisor at DLR: Dr. Victor Zhukov

Second supervisor at DLR: Jan Van Schnydel, M.Sc.

June 30, 2018



# **Optimized Meshing for Rocket Combustion Chambers Simulations**

**Henrique Alas Martins Cestaro**

Mestrado em Mecânica Computacional

June 30, 2018



# Resumo

Em simulações CFD de câmaras de combustão de foguetes, a malha utilizada tem influência na forma da chama; quanto mais refinada a malha, mais longa é a chama. Uma estratégia pra eliminar essa fonte de erros numéricos é criar uma malha suficientemente refinada de forma que um refinamento adicional não altere a solução obtida. Essa estratégia cria malhas grandes, que demandam muito tempo para serem resolvidas. Outra possível estratégia é a utilização de algoritmos de adaptação de malha, refinando apenas as regiões críticas da malha. Nesse trabalho, métodos de adaptação de malha foram testados em diferentes câmaras de combustão de foguetes, utilizando o código comercial ANSYS CFX e o código desenvolvido internamente pela DLR, o TAU code. Simulações foram feitas para otimizar os valores dos parâmetros de adaptação de ambos os programas. Foi observado que, para os casos estudados, as simulações no ANSYS CFX produziram chamas com comprimentos próximos aos esperados em malhas refinadas uniformemente, enquanto as simulações utilizando o TAU code tiveram chamas até 15% maiores do que o esperado para malhas com refinamento regular e similar espaçamento médio.



# Abstract

In the CFD simulations of rocket combustion chambers, the mesh has an impact on the shape of the flame; the finer the mesh, the longer the flame. A possible approach to eliminate this source of numerical error is to create a mesh sufficiently refined that further refinement will lead to no difference on the solution. This approach can create large meshes, that are time consuming to solve. Another approach is to use mesh adaptation algorithms, to refine only the critical region of the mesh. In this work, mesh adaptation methods have been tested for different rocket combustion chamber cases, using the commercial code ANSYS CFX and the in-house CFD code of DLR, the TAU code. Simulations were performed to optimize the values of the adaptation parameters of both software. It was observed that, for the studied case, the ANSYS CFX simulations had a flame length similar to the expected from a uniformly refined mesh, while the simulation using the TAU code had flames up to 15% longer than the expected for a uniformly refined mesh with similar mean mesh spacing.





# Contents

<b>1</b>	<b>Introduction</b>	<b>1</b>
<b>2</b>	<b>Methods</b>	<b>3</b>
2.1	Governing equations and CFD . . . . .	3
2.1.1	Time- and Favre-Averaging . . . . .	4
2.1.2	Turbulence model . . . . .	5
2.1.3	Reactive flow . . . . .	7
2.2	ANSYS CFX simulations . . . . .	8
2.2.1	API geometry . . . . .	8
2.2.2	API mesh . . . . .	9
2.2.3	ANSYS CFX simulation parameters . . . . .	10
2.3	TAU code simulations . . . . .	13
2.3.1	Coaxial injector geometry . . . . .	13
2.3.2	Coaxial injector mesh . . . . .	14
2.3.3	TAU code simulations parameters . . . . .	16
2.4	Mesh adaptation . . . . .	16
2.4.1	ANSYS CFX mesh adaptation . . . . .	17
2.4.2	TAU code mesh adaptation . . . . .	18
2.4.3	Adaptation approach . . . . .	19
<b>3</b>	<b>Results and discussions</b>	<b>23</b>
3.1	ANSYS CFX simulations . . . . .	23
3.1.1	ANSYS CFX reference meshes . . . . .	23
3.1.2	ANSYS CFX mesh adaptation parameters . . . . .	26
3.1.3	ANSYS CFX simulation results . . . . .	34
3.1.4	ANSYS CFX simulations conclusions . . . . .	36
3.2	TAU code simulations . . . . .	38
3.2.1	TAU code reference meshes . . . . .	38
3.2.2	TAU code mesh adaptation parameters . . . . .	40
3.2.3	TAU code simulation results . . . . .	48
3.2.4	TAU code simulations conclusions . . . . .	50
<b>4</b>	<b>Conclusions</b>	<b>51</b>
<b>A</b>	<b>List of ANSYS CFX adaptation simulations</b>	<b>53</b>
<b>B</b>	<b>List of TAU code adaptation simulations</b>	<b>59</b>



# List of Figures

2.1	Control volume [3] . . . . .	4
2.2	The API-68 porous injector head. [7] . . . . .	9
2.3	API-68 injectors arrangement and simulated injector. . . . .	9
2.4	Schematic front view of the injector. . . . .	10
2.5	Schematic bottom view of the injector. . . . .	11
2.6	Mesh at the injector tip region, plane $xz$ : (a) mesh AO1, (b) mesh AO2, (c) mesh AO3 and (d) mesh AO4. . . . .	12
2.7	Mesh at the transition region at the downstream end of the refinement region, plane $xz$ : (a) mesh AO1, (b) mesh AO2, (c) mesh AO3 and (d) mesh AO4. . . . .	13
2.8	Geometry of the simulated coaxial injector. . . . .	14
2.9	Measures of the adapted region on the coaxial injector. . . . .	14
2.10	2D mesh at the injector region: (a) mesh TO1, (b) mesh TO2, (c) mesh TO3 . . . .	15
2.11	Flowchart of an ANSYS CFX mesh adaptation process. Adapted from [2] . . . . .	18
3.1	Temperature distribution on the $x$ - $z$ base plane for the ANSYS CFX reference meshes and a black line at $T = 2000$ K. From top to bottom, meshes AO1, AO2, AO3 and AO4. . . . .	24
3.2	Temperature distribution along a central line for the ANSYS CFX reference meshes simulations. . . . .	25
3.3	ANSYS CFX reference curve fit for flame length. . . . .	25
3.4	Radial evolution of temperature, $H_2$ , $O_2$ and $H_2O$ molar fractions along a line parallel to the faceplate, distant 15 mm, for the AO1 mesh. . . . .	26
3.5	Flame length for ANSYS CFX simulations compared to the reference curve: (a) absolute values, (b) relative values. . . . .	28
3.6	Comparison of $F_{rel}$ for different values of "variable list". . . . .	29
3.7	Comparison of $F_{rel}$ for different values of "adaptation method". . . . .	30
3.8	Comparison of $F_{rel}$ for different values of "node allocation". . . . .	31
3.9	Comparison of $F_{rel}$ for different values of "number of levels". . . . .	33
3.10	ANSYS CFX simulations with the largest and smallest reference flame length. . . .	35
3.11	Temperature distribution, a line of $T = 2000$ K and the mesh of the simulations A_EV_01 (top) and A_T.H2O.H2_02 (bottom). . . . .	36
3.12	Temperature distribution along a central line for the best, worst and reference ANSYS CFX simulations. . . . .	37
3.13	Temperature distribution for the TAU code reference meshes and a black line at $T=2000$ K. From top to bottom, TO1, TO2, TO3. The axial direction is clinched by a factor of 2. . . . .	38
3.14	Temperature distribution along a central line for the TAU code reference meshes simulations. . . . .	39

3.15	TAU code reference curve fit for flame length. . . . .	39
3.16	Radial evolution of temperature and species mass fractions along a line parallel to the faceplate, distant 60 mm, for the TO1 mesh. . . . .	40
3.17	Flame length for TAU code simulations compared to the reference curve: (a) absolute values, (b) relative values. . . . .	42
3.18	Comparison of $F_{rel}$ for different values of "indicator user-values". . . . .	43
3.19	Comparison of $F_{rel}$ for different values of "indicator type". . . . .	44
3.20	Comparison of $F_{rel}$ for different values of "h-scaling power". . . . .	45
3.21	Comparison of $F_{rel}$ for different values of "percentage of new points". . . . .	46
3.22	TAU code simulations with the largest and smallest reference flame length. . . . .	48
3.23	Temperature distribution, a line of $T = 2000$ K and the mesh of the simulations T_T_diff_100i_300s (top), T_T_recon_a1_75.5.5_3s (middle) and T_H2_diff_3s (bottom). The axial direction is clinched by a factor of 2. . . . .	49
3.24	Temperature distribution along a central line for the best, worst and reference TAU code simulations. . . . .	50

# List of Tables

2.1	Summary of the API computational domain measures. . . . .	9
2.2	Summary of meshes used for ANSYS CFX simulations. . . . .	10
2.3	Boundary conditions for the ANSYS CFX simulations. [24] . . . . .	11
2.4	Summary of the coaxial injector computational domain measures. . . . .	15
2.5	Summary of meshes used for the TAU code simulations. . . . .	15
2.6	Boundary condition for the TAU code simulations. . . . .	16
3.1	Summary of flame length for ANSYS CFX reference meshes. . . . .	24
3.2	Tested values for ANSYS CFX adaptation parameters. . . . .	27
3.3	Parameters of the simulation for "adaptation method" tests. . . . .	30
3.4	Parameters of the simulations for "node allocation" tests. . . . .	31
3.5	Parameters of the simulations for "number of levels" tests. . . . .	32
3.6	Parameters of the simulations for "maximum number of steps" tests. . . . .	32
3.7	Best values for ANSYS CFX adaptation parameters. . . . .	33
3.8	ANSYS CFX adaptation simulations with the largest and smallest relative flame lengths. . . . .	35
3.9	Summary of flame length for TAU code reference meshes. . . . .	39
3.10	Tested values for TAU code mesh adaptation. . . . .	41
3.11	Parameters of the simulations for "indicator type" tests. . . . .	43
3.12	Parameters of the simulations for "h-scaling power" tests. . . . .	45
3.13	Parameters of the simulations for "percentage of new points" tests. . . . .	46
3.14	Best values for TAU code adaptation parameters. . . . .	47
3.15	Parameters for the TAU code dynamical simulations . . . . .	47
3.16	TAU code reference meshes and adaptation simulations with the largest and smallest relative flame lengths. . . . .	49
4.1	Best values for ANSYS CFX adaptation parameters. . . . .	52
4.2	Best values for TAU code adaptation parameters. . . . .	52



# Abbreviations and Symbols

## Symbols

$A$	$[\text{m}^3 \text{mol}^{-1} \text{s}^{-1}]$	Pre-exponential factor
$A_e$	[-]	Adaptation criteria for the edge $e$
$c_i$	$[\text{kg m}^{-3}]$	Mass concentration of the component $i$
$c_{cond}$	$[\text{W m}^{-2} \text{K}^{-1}]$	Conduction coefficient
$d_w$	[mm]	Wall thickness
$e$	[-]	Element edge
$E_a$	$[\text{J mol}^{-1}]$	Reaction activation energy
$F_i$	[mm]	Flame length for case $i$
$F_{i,j}$	[-]	Increase of flame length in case $i$ compared to case $j$
$F_{rel}$	[-]	Relative flame length
$h$	[mm]	Average mesh spacing
$h_{tot}$	$[\text{m}^2 \text{s}^{-2}]$	Total enthalpy
$l$	[mm]	Length of cell edge
$k$	$[\text{m}^2 \text{s}^{-2}]$	Turbulence kinetic energy
$k_r$	$[\text{m}^3 \text{mol}^{-1} \text{s}^{-1}]$	Reaction rate constant
$Pr_{tr}$	[-]	Turbulent Prandtl number
$q$	$[\text{W m}^2]$	Heat flux
$R$	$[\text{J mol}^{-1} \text{K}^{-1}]$	Universal gas constant
$Sc_{tr}$	[-]	Turbulent Schmidt number
$S_E$	$[\text{W m}^{-3}]$	Energy source
$S_M$	$[\text{N m}^{-3}]$	Momentum source
$S_A$	$[\text{kg m}^{-3} \text{s}^{-1}]$	Component A source
$t$	[s]	Time
$T$	[K]	Temperature
$T_r$	[K]	Reservoir temperature
$T_w$	[K]	Wall temperature
$\mathbf{u}$	$[\text{m s}^{-1}]$	Velocity vector
$\mathbf{x}_{pi}$	[mm]	Position vector of the point $i$
$v$	$[\text{m s}^{-1}]$	$y$ component of the velocity vector
$V$	$[\text{m}^3]$	Volume
$w$	$[\text{m s}^{-1}]$	$z$ component of the velocity vector
$y^+$	[-]	Dimensionless wall distance
$Y_A$	[-]	Mass fraction of component A in the fluid
$\alpha$	[-]	Edge length scaling factor
$\Gamma_A$	$[\text{kg m}^{-1} \text{s}^{-1}]$	Molecular diffusion coefficient of component A
$\delta$	[-]	Identity matrix

$\varepsilon$	$[\text{m}^2 \text{s}^{-3}]$	Turbulence dissipation rate
$\lambda$	$[\text{W m}^{-1} \text{K}^{-1}]$	Thermal conductivity
$\lambda_w$	$[\text{W m}^{-1} \text{K}^{-1}]$	Wall thermal conductivity
$\mu$	$[\text{Pa s}^{-1}]$	Dynamic viscosity
$\mu_{eff}$	$[\text{Pa s}^{-1}]$	Effective viscosity
$\mu_t$	$[\text{Pa s}^{-1}]$	Turbulent viscosity
$\nu$	$[\text{m}^2 \text{s}^{-1}]$	Kinematic viscosity
$\rho$	$[\text{kg m}^{-3}]$	Density
$\tau$	$[\text{Pa}]$	Stress tensor
$\phi$	$[-]$	General scalar variable
$\omega$	$[\text{Hz}]$	Turbulent frequency

## Abbreviations

API	Advanced Porous Injector
DLR	Deutsches Zentrum für Luft- und Raumfahrt (German Aerospace Center)
CFD	Computational Fluid Dynamics
EDM	Eddy Dissipation Model
FANS	Favre-averaged Navier-Stokes
RANS	Reynolds-averaged Navier-Stokes
SST	Shear Stress Transport
ROF	Mass ratio of oxidizer-to-fuel



# Chapter 1

## Introduction

Sending payloads to space or high atmosphere requires the use of rockets. For scientific, military and commercial purposes, there is a constant need for rocket engines with high efficiency and reliability. Constant research is the key for increasing the knowledge about the components and phenomena that take part on them, allowing the development of better engines. These researches can be done by experimental tests, which are expensive and time demanding, or by computational simulations, that are cheaper and faster but need an advance development.

Computational Fluids Dynamics (CFD) has had a great development concomitant with a increase in computing capacity and decrease in computational costs. It is used in many applications, including combustion modelling and rocket engine research. The use of CFD can save time and money during the development process, decreasing the need of hot-fire tests, and increasing the variety of possible studies. With CFD it is possible to simulate multiple cases simultaneously, testing a wider range of configurations and designs. The results of CFD simulations may vary a lot, according to the models applied, the mesh and the type of simulation, [19, 23, 22] and therefore an evaluation phase is always necessary to improve the numerical model, cross checking the numerical results with analytical or experimental ones. After the evaluation phase the numerical results can be considered to represent the real phenomena.

One type of error on CFD simulations is the spatial discretization error, due to the partitioning of the computational domain into a mesh. The results are influenced by the kind of elements that are used, their refinement (amount of nodes) and their distribution. One way of estimating the mesh influence on the final solution is performing a grid convergence study, using multiple meshes with different refinement levels to compare their influence on the final result and extrapolate the result for a case of a "zero" spacing mesh, [1].

Regions where the variable have higher gradients tend to have higher error, therefore they require finer meshes to describe to problem properly. Sometimes theses regions are known *a priori* and the mesh can be created taking this into account, but often the higher gradient regions are unknown. Optimizing the mesh in these cases requires iterative processes, adapting the mesh according to the previous solution, [9, 8].

The effect of the mesh spacing on combustion chamber simulation results has been evaluated

for different combustors [23, 4]. It has been observed to have an influence on the flame length and the wall heat flux with the mesh refinement. Different approaches have been used for mesh adaption for combustion simulation, [5, 10],

For the combustion in rocket engines, fuel and oxidizer must be mixed before ignition and combustion. For a better control of the combustion and the flame, the fuel and the oxidizer must be injected separately and then mixed inside the combustion chamber, just before the ignition. The type of injector mainly used for oxygen/hydrogen combustion is the coaxial injector, that consists in two pipes, one inside the other, one for oxygen and other for hydrogen injection. Several injectors can be used in a single engine.

In these injectors, liquid oxygen (LOx) is injected by the inner injector into a gaseous hydrogen surrounding. The shear layer between the liquid surface and the gaseous environment causes instabilities and the liquid is broken down into small drops. These drops evaporate and, together with the fuel, form a mixture that can be efficiently burned, [12].

On rocket engine design, operational flexibility is a key requirement for an useful injector head, that is, it has to be capable of operating in a broad range of thrust level without major degradation of the combustion efficiency and combustion stability. Coaxial injectors are efficient in a narrow range of mass flows, and require a very precise manufacturing. The use of porous materials can be a solution for both problems decreasing manufacturing costs and maintaining the efficiency over a wide throttling range, from 37.5% to 125% [6].

A concept of a porous injector has been studied at the Institute of Space Propulsion of the German Aerospace Center (DLR-Lampoldshausen) [6, 16, 7], with the development of an Advanced Porous Injector (API). On the API, liquid oxygen is injected through a large number of simple tubes, while hydrogen is injected through the porous face plate. Porous injector heads operate at smaller pressure drops than coaxial injectors and they also have a smaller jet break-up distance, allowing a reduction in the combustion chamber length, decreasing the total mass and improving the performance of the rocket engine.

The present research was developed at the Institute of Space Propulsion of DLR. This work aims in developing a procedure for mesh optimization of rocket combustion chambers operating with oxygen and hydrogen. API and coaxial combustion chambers will be used for this developing, and the final procedure have to be easy to use, with as few steps as possible. The optimized parameter will be the relation between the flame length and the number of nodes on the final mesh. Simulation will be performed using the commercial CFD code ANSYS CFX and the in-house CFD code of DLR, TAU code.

# Chapter 2

## Methods

### 2.1 Governing equations and CFD

Any fluid flow is ruled by the fundamental physical principle of conservation of mass, conservation of momentum and conservation of energy. From these three principles it is possible to derive the governing equations of fluid motion: the continuity equation (2.1), the momentum equation (2.2) and the energy equation (2.3), [14]. These equations are also called the Navier-Stokes equations.

$$\underbrace{\frac{\partial \rho}{\partial t}}_I + \underbrace{\nabla \cdot (\rho \mathbf{u})}_{II} = 0 \quad (2.1)$$

$$\underbrace{\frac{\partial (\rho \mathbf{u})}{\partial t}}_{III} + \underbrace{\nabla \cdot (\rho \mathbf{u} \otimes \mathbf{u})}_{IV} = - \underbrace{\nabla p}_V + \underbrace{\nabla \cdot \boldsymbol{\tau}}_{VI} + \underbrace{\mathbf{S}_M}_{VII} \quad (2.2)$$

$$\underbrace{\frac{\partial h_{tot}}{\partial t} - \frac{\partial p}{\partial t}}_{VIII} + \underbrace{\nabla \cdot (\rho \mathbf{u} h)}_{IX} = \underbrace{\nabla \cdot (\lambda \nabla T)}_X + \underbrace{\nabla \cdot (\mathbf{u} \cdot \boldsymbol{\tau})}_{XI} + \underbrace{\mathbf{S}_E}_{XII} \quad (2.3)$$

where  $\boldsymbol{\tau}$  is the stress tensor and is given by (2.4); I, III and VIII are the internal changes on the fluid; II, IV and IX are the changes due to the flow over the boundary; V pressure gradient acting on the fluid surface; VI is the shear stress also acting on the fluid surface; VII are the sources of momentum; X are the energy changes due to heat conduction; XI is the work due to viscous stress; and XII are the sources of energy.

$$\boldsymbol{\tau} = \mu \left( \nabla \mathbf{u} + (\nabla \mathbf{u})^T - \frac{2}{3} \delta \nabla \cdot \mathbf{u} \right) \quad (2.4)$$

Analytical solutions for these equations are known only for the simplified flows under ideal conditions. For real flows a numerical approach must be used and the governing equations are replaced by algebraic approximations that can be solved by numerical methods. Solving the analytical approximation of the governing equations must be done in an discretized domain, that is,

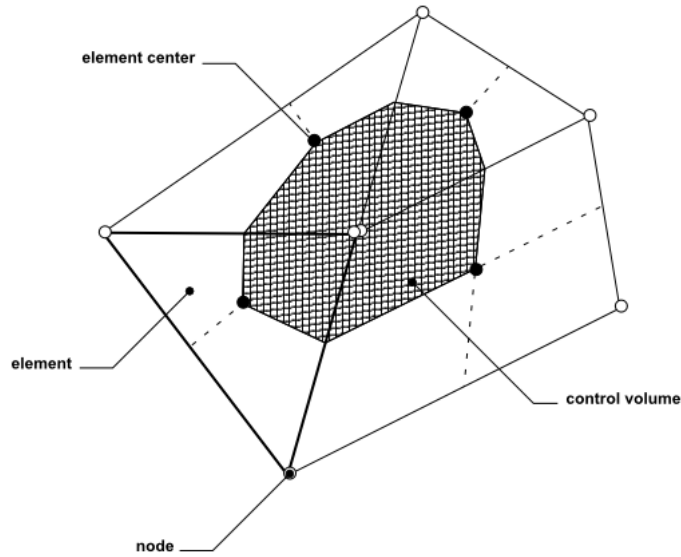


Figure 2.1: Control volume [3]

in a grid of points approximated from the continuum domain. The equations will then be solved only for these points (or nodes), from which other points' solution can be interpolated.

On CFD applications the *finite volume* method is usually used. In this method control volumes are created around each mesh node, the governing equations are integrated on each volume and the solution variables and fluid properties are stored on the nodes. An example of a 2D control volume is shown in Figure 2.1.

### 2.1.1 Time- and Favre-Averaging

In principle, it is possible to solve the Navier-Stokes equations for any kind of flow, laminar or turbulent, using *direct numerical simulation* (DNS). In practice, turbulent flows solution, are computational prohibitive. For a DNS it is necessary to have a grid with a resolution capable of solving all the small scales of the turbulence, demanding more computational time and capacity than it is reasonable, or even available nowadays. Besides that, solving the time dependent Navier-Stokes equation for every instant in time might be of little practical interest, since often the important information can be obtained from a time averaged solution.

One approach to solve the time dependence of the variables is assuming the flow to be chaotic process that can be described by an average property with a fluctuating component. With the *time-averaging* (or Reynolds-averaging), (2.5), it is possible to separate the turbulent fluctuations from the mean-flow. The Reynolds-averaged Navier-Stokes (RANS) equations are obtained when time-averaging the flow governing equations.

$$\bar{\phi} = \frac{1}{\Delta t} \int_t^{t+\Delta t} \phi(t) dt \quad (2.5)$$

$$\phi' = \phi - \bar{\phi} \quad \text{and} \quad \bar{\phi}' = 0$$

In situations of large density variations, like in combustion simulations, the flow properties should also be *density-weighted averaged*, (2.6). Density-weighted averaging, or *Favre averaging*, is used to separate the turbulent fluctuations from the mean-flow on a highly compressible flows and hypersonic flows. The Favre-averaged Navier-Stoke (FANS) equations can be derived in a similar way to the RANS equations.

$$\begin{aligned}\tilde{\phi} &= \frac{\overline{\rho\phi}}{\bar{\rho}} \\ \phi'' &= \phi - \tilde{\phi} \quad \text{and} \quad \overline{\rho\phi''} = 0\end{aligned}\tag{2.6}$$

From (2.5) and (2.6) is possible to calculate the Favre average from the average of variable  $\phi$ .

$$\begin{aligned}\tilde{\phi} &= \frac{\overline{\rho\phi}}{\bar{\rho}} = \frac{(\bar{\rho} + \rho')(\bar{\phi} + \phi')}{\bar{\rho}} = \frac{\overline{\rho\phi} + \overline{\rho\phi'} + \overline{\rho'\phi} + \overline{\rho'\phi'}}{\bar{\rho}} \\ &\Rightarrow \tilde{\phi} = \bar{\phi} + \frac{\overline{\rho'\phi'}}{\bar{\rho}}\end{aligned}\tag{2.7}$$

The value of  $\overline{\rho'\phi'}$  must be known and it usually is calculated from the conservation equation.

### 2.1.2 Turbulence model

Averaging the Navier-Stokes equations introduces additional unknown terms containing products of the fluctuating quantities, on the form of  $\overline{\rho\mathbf{u}''\phi''}$ , which act like additional stress on the fluid. These terms, called 'turbulent' or 'Reynolds' stresses, need to be modelled by additional equations of the known properties for the problem to be solvable.

One approach to model this additional equations is to consider the turbulence as small eddies that are continuously forming and dissipating, and can be described by an eddy viscosity,  $\mu_t$ . This is comparable on how the momentum transfer caused by the molecular motion in a gas is described by a molecular (or dynamic) viscosity,  $\mu$ . The *eddy viscosity models* replace the dynamic viscosity on the averaged Navier-Stokes equations by an effective viscosity,  $\mu_{eff}$ , (2.8).

$$\mu_{eff} = \mu + \mu_t\tag{2.8}$$

With  $\mu_t$  an additional variable is added, so that a further equation is required to solve the problem. Several RANS based turbulences models, with different approaches are available. The *two-equation turbulence models* offer a good compromise between numerical effort and numerical accuracy. In these models, the turbulent viscosity is modelled as a function of the flow properties, as presented in (2.9) and (2.12), which then is solved using separate transport equations. The turbulent velocity scale is computed from the turbulent kinetic energy. The turbulent length scale is estimated from two properties of the turbulence field, usually the turbulent kinetic energy and its dissipation rate. Both the turbulent kinetic energy and its dissipation rate are obtained from their own transport equations.

The turbulent kinetic energy,  $k$ , is the variance of the fluctuation in velocity, the turbulence eddy dissipation,  $\varepsilon$ , is the rate at which the velocity fluctuations dissipate and  $\omega$  is the turbulent frequency.

### 2.1.2.1 $k - \varepsilon$ turbulence model

The  $k - \varepsilon$  turbulence model solves two transport equations, one for  $k$ , (2.10) and other for  $\varepsilon$ , (2.11). Generally, it has good results far from walls and for fully turbulent flows. The eddy viscosity is given by (2.9).

$$\mu_t = C_\mu \rho \frac{k^2}{\varepsilon} \quad (2.9)$$

$$\frac{\partial(\rho k)}{\partial t} + \nabla \cdot (\rho \mathbf{u} k) = \nabla \cdot \left[ \left( \mu + \frac{\mu_t}{\sigma_k} \right) \nabla k \right] + P_k + P_{kb} - \rho \varepsilon \quad (2.10)$$

$$\frac{\partial(\rho \varepsilon)}{\partial t} + \nabla \cdot (\rho \mathbf{u} \varepsilon) = \nabla \cdot \left[ \left( \mu + \frac{\mu_t}{\sigma_\varepsilon} \right) \nabla \varepsilon \right] + \frac{\varepsilon}{k} (C_{\varepsilon 1} (P_k + P_{\varepsilon b}) - C_{\varepsilon 2} \rho \varepsilon) \quad (2.11)$$

where  $C_{\varepsilon 1}$ ,  $C_{\varepsilon 2}$ ,  $\sigma_k$  and  $\sigma_\varepsilon$  are model constants,  $P_{kb}$ ,  $P_{\varepsilon b}$  represent the influence of the buoyancy force and  $P_k$  is the turbulence production due to viscous forces.

### 2.1.2.2 $k - \omega$ turbulence model

The  $k - \omega$  turbulence model is based on the transport equations for  $k$  and  $\omega$ , (2.13) and (2.14). It has better results near walls and for low-Reynolds number simulations. The eddy viscosity is given by (2.12).

$$\mu_t = \rho \frac{k}{\omega} \quad (2.12)$$

$$\frac{\partial(\rho k)}{\partial t} + \nabla \cdot (\rho \mathbf{u} k) = \nabla \cdot \left[ \left( \mu + \frac{\mu_t}{\sigma_k} \right) \nabla k \right] + P_k + P_{kb} - \beta' \rho k \omega \quad (2.13)$$

$$\frac{\partial(\rho \omega)}{\partial t} + \nabla \cdot (\rho \mathbf{u} \omega) = \nabla \cdot \left[ \left( \mu + \frac{\mu_t}{\sigma_\omega} \right) \nabla \omega \right] + \alpha \frac{\omega}{k} P_k + P_{\omega b} - \beta \rho \omega^2 \quad (2.14)$$

where  $\beta'$ ,  $\alpha$ ,  $\beta$ ,  $\sigma_\omega$  are model constants and  $P_{\omega b}$  is the turbulent buoyancy.

### 2.1.2.3 Shear Stress Transport model

The Shear Stress Transport model (SST) combines the  $k - \omega$  model near walls and the  $k - \varepsilon$  model for the free-stream region. The  $k - \omega$  model is multiplied by a blending function  $F_1$ , (2.17) and the  $k - \varepsilon$  model is transformed to a  $k - \omega$  formulation and then multiplied by  $(1 - F_1)$ . The blending function  $F_1$  is equal to one near the wall and decrease to a value near zero outside the boundary layer.

The eddy viscosity is calculated by (2.15) and (2.16).  $F_2$  is a second blending function, with a behaviour similar to  $F_1$ .

$$\nu_t = \frac{a_1 k}{\max(a_1 \omega, S F_2)} \quad (2.15)$$

$$\nu_t = \frac{\mu_t}{\rho} \quad (2.16)$$

$$F_1 = \tanh \left\{ \left\{ \min \left[ \max \left( \frac{\sqrt{k}}{\beta' \omega y}, \frac{500 \nu}{y^2 \omega} \right), \frac{4 \rho k}{C D_{k\omega} \sigma_{\omega 2} y^2} \right] \right\}^4 \right\} \quad (2.17)$$

$$F_2 = \tanh \left[ \left[ \max \left( \frac{2\sqrt{k}}{\beta' \omega y}, \frac{500 \nu}{y^2 \omega} \right) \right]^2 \right] \quad (2.18)$$

where  $a_1$ ,  $\sigma_{\omega 2}$  are constants,  $S$  is an invariant measure of the strain rate,  $y$  is the distance to the nearest wall and:

$$C D_{k\omega} = \max \left( 2\rho \frac{1}{\sigma_{\omega 2} \omega} \nabla k \omega, 1.0 \times 10^{-10} \right) \quad (2.19)$$

### 2.1.3 Reactive flow

On a reacting flow it is still necessary to specify the averaged chemical reaction rates, for further calculation of the density and pressure and the complete solution of the averaged conservation equations. In contrast to normal CFD, the normal density equation and  $(n-1)$  transport equations, (2.20), must be solved for the full solution of the problem.

$$\underbrace{\frac{\partial (\rho Y_A)}{\partial t}}_I + \underbrace{\frac{\partial (\rho u_j Y_A)}{\partial x_j}}_{II} = \underbrace{\frac{\partial}{\partial x_j} \left( \Gamma_{Aeff} \frac{\partial Y_A}{\partial x_j} \right)}_{III} + \underbrace{S_A}_{IV} \quad (2.20)$$

where I is internal change on the fluid; II the change due to the flow over the boundaries; III is the change due to diffusivity; and IV is the rate of production/consumption of species A and is given by a function of the reaction rate constants,  $k_r$ , and the concentration of the species for each reaction, as shown in (2.21)

$$S_A = f(k_r, c_A, c_B, \dots) \quad (2.21)$$

For the calculation of  $k_r$  two different models are presented.

#### 2.1.3.1 Eddy Dissipation Model

The Eddy Dissipation Model (EDM) is an empirical model used in cases where the the chemical reaction is considered to be fast relative to the transport processes in the flow. The reaction

rate is governed by the rate of turbulent dissipation, (2.22), and is an example of *mixed-is-burnt* combustion model class.

$$k_r \propto \frac{\varepsilon}{k} \quad (2.22)$$

The EDM can be applied for the hydrogen combustion, since in this combustion the effect the kinetic model is insignificant, as the chemical timescales are considerably smaller than the flow and turbulent time-scales [13]. This model tends to over-predict the temperatures and concentration of species in the reaction zone, however it is a popular model due to its simplicity, steady convergence and easy implementation.

### 2.1.3.2 Finite rate chemistry model

The finite rate chemistry model is based on the Arrhenius equation, (2.23). It assumes that reactions are reversible, with different reactions rates, for forward and backward reaction. The forward reaction rates are calculated using the modified Arrhenius equation, and the backward reaction rates are calculated over an equilibrium constant. The final reaction rate is a sum of all forward and the backward rates.

$$k_r = AT^n e^{-E_a/(RT)} \quad (2.23)$$

where  $A$ ,  $n$  and  $E_a$  are given constants for each reaction.

## 2.2 ANSYS CFX simulations

### 2.2.1 API geometry

One of the simulated combustion chamber uses an Advanced Porous Injector with 68 LOx injectors, the API-68 injector head – more details on this injector are available in [6, 7, 25, 24]. The API-68, presented in Figure 2.2, consists of a porous plate sintered from bronze beads. The plate is permeated by 68 practically uniformly distributed stainless steel tubes of small diameter. These tubes have a plain geometry, and are sharp cut (no tapering nor recess). Oxygen is injected through these tubes, while hydrogen is fed uniformly through the porous plate. The oxygen and hydrogen inlet are separated by a small ring, the injector tip.

The API simulations were done using ANSYS CFX software. The three-dimensional computational domain consists of half an oxygen injector from the API-68, Figure 2.3. An injector in the central region of the API was chosen due to its symmetry, being easier to simulate. The boundaries of the simulated region are defined by the mid points to the neighbouring injectors. The result is a right triangle with sides of approximately  $5 \times 5 \times 5\sqrt{2}$  mm. The oxygen injector has an inner and outer diameters of 1.5 mm and 2 mm, respectively. The LOx injector is modelled with a length of 15 mm upstream of the injector plate, to allow the formation of a realistic exit velocity profile within the boundary layer at the wall. The modelled part of the combustion chamber has an length





Figure 2.2: The API-68 porous injector head. [7]

of 225 mm. The front and bottom views of the domain are presented in Figures 2.4 and 2.5. A summary of the measures on the injector is presented in Table 2.1.

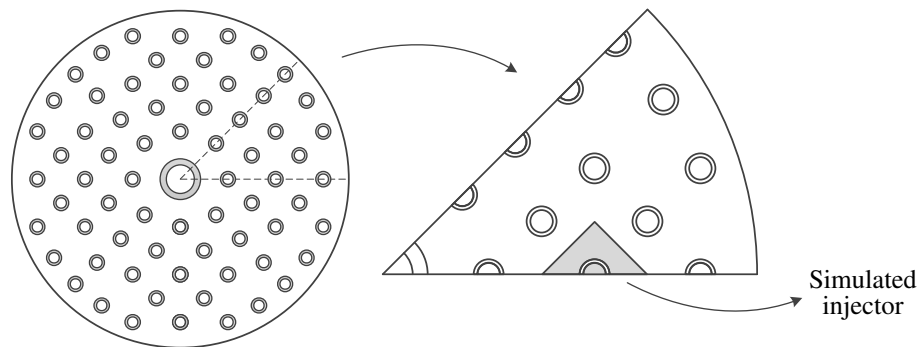


Figure 2.3: API-68 injectors arrangement and simulated injector.

Table 2.1: Summary of the API computational domain measures.

LOx injector outer diameter	1.5 mm
LOx injector inner diameter	2 mm
LOx injector length	15 mm
Sides length	$5 \times 5 \times 5\sqrt{2}$ mm
Combustion chamber length	225 mm

### 2.2.2 API mesh

The initial mesh used for the API combustion chamber simulations is one of the meshes used by Zhukov and Heinrich, [23], with 300 thousand nodes and 1.45 million volume elements. The unstructured 3D mesh was created using the software ANSYS ICEM CFD and is composed mainly by tetrahedral elements, with a prismatic layers inflation in the oxygen injector wall and tip. A

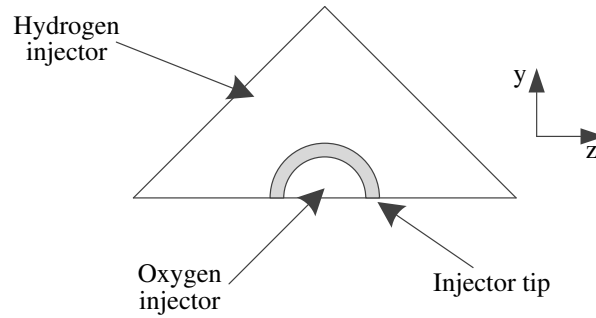


Figure 2.4: Schematic front view of the injector.

refinement region was created within the first 50 mm of the combustion chamber, decreasing significantly the edges lengths in this region. The transitions between this density region and its surroundings was made by a gradual growth of the elements.

The adaptation process was performed on the mesh with 301 thousand nodes (named AO1), and the results are compared with other 3 meshes used by Zhukov and Heinrich. All the meshes are based on the AO1 mesh, using scale factors to decrease the edge length uniformly all over the domain. The average mesh spacing,  $h$ , is calculated via (2.24) for each mesh, [1]. In (2.24)  $N$  is the total number of elements and  $V_i$  is the element volume. The meshes summary is presented in Table 2.2 whereas Figures 2.6 and 2.7 show the regions of interest for the four different meshes.

$$h = \left[ \frac{1}{N} \sum_{i=1}^N \Delta V_i \right]^{1/3} \quad (2.24)$$

### 2.2.3 ANSYS CFX simulation parameters

The boundary conditions used for the simulations of the API chamber are the same as used by Zhukov and Heinrich, [23]. The inlet and outlet values are presented in Table 2.3. The oxygen injector wall is considered as a smooth no slip wall with a fixed temperature of 180 K. The injector tip is a free slip wall, also with fixed a temperature of 180 K. The side walls of the domain are all considered to be symmetry walls.

Table 2.2: Summary of meshes used for ANSYS CFX simulations.

Mesh	Number of nodes	Number of elements	$h$ [mm]
AO1	300 k	1.45 M	0.125
AO2	385 k	2.05 M	0.111
AO3	651 k	3.51 M	0.093
AO4	1.128 M	6.16 M	0.077

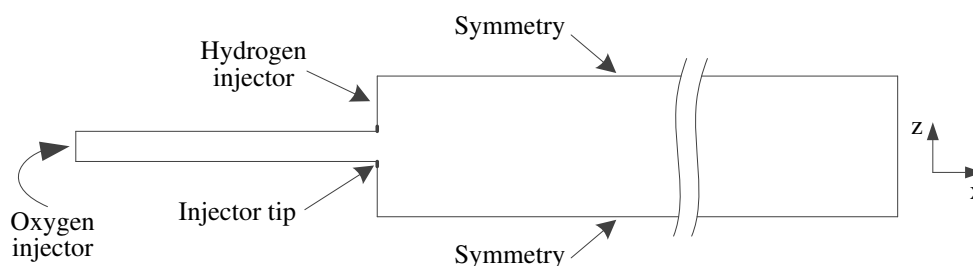


Figure 2.5: Schematic bottom view of the injector.

The flow is modelled using the Favre-averaged Navier-Stokes equations, the turbulence is modelled using the SST turbulence model and the combustion was modelled using an extended EDM. All governing equation, except the equations for enthalpy and for mass fraction of the mixture components have been solved using the "High Resolution" advection scheme. The equations for enthalpy and for the mass fractions of mixture components have been solved using the first order upwind differencing scheme. The first order scheme was used due to divergences in the solver when using high resolution scheme [23].

Turbulent combustion was modelled using an extended EDM model, following the recommendations of Zhukov, [22]. Chemical reactions occurs in a single-step global reaction, with only three species –  $H_2$ ,  $O_2$  and  $H_2O$ .



At high temperatures ( $T > 3000$  K) the dissociation of  $H_2O$  becomes important, that is, the fraction of  $H_2O$  in the burned gases of a rocket combustion chamber is significantly less than 100%. The rate of chemical reaction is limited by a "maximum flame temperature" parameter, making the reaction rate to be set to zero when the reaction mixture reaches this limit temperature. The value of maximum flame temperature is precalculated using the program NASA Chemical Equilibrium with Applications (CEA) [18].

Two additional parameter were added to this extended EDM, for an accurate modelling of the interaction between flame and turbulence. Near the wall the turbulent mixing rate  $\epsilon/k$  becomes larger, due to an decrease of the turbulent kinetic energy  $k$ . To avoid the reaction rate going unnaturally high, a maximum value of  $\epsilon/k$  is set by a parameter "mixing rate limit". Also, in

Table 2.3: Boundary conditions for the ANSYS CFX simulations. [24]

Injection velocity, $O_2$	13.56 m/s
Temperature, $O_2$	120 K
Injection velocity, $H_2$	9.10 m/s
Temperature, $H_2$	100 K
Mass ratio of oxidizer-to-fuel (ROF)	6
Pressure at the outlet	$\approx 75.5$ bar

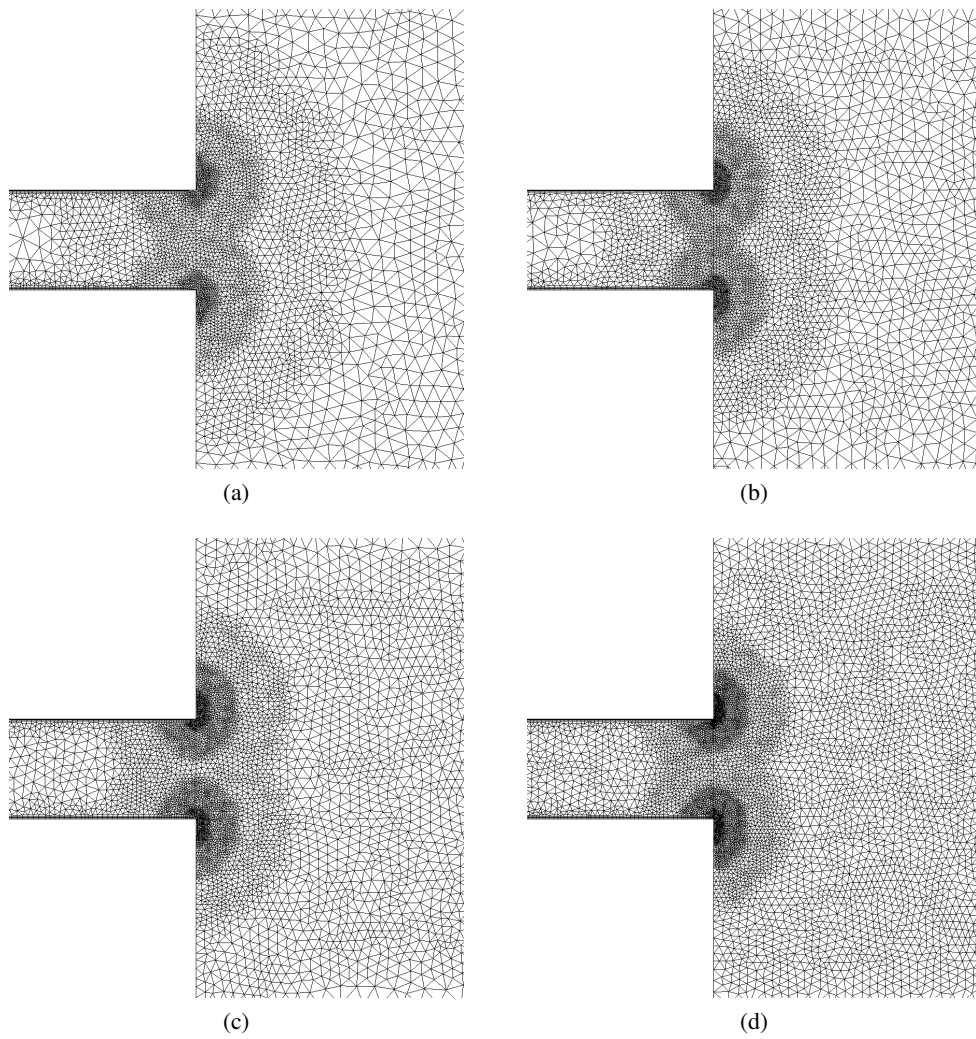


Figure 2.6: Mesh at the injector tip region, plane  $xz$ : (a) mesh AO1, (b) mesh AO2, (c) mesh AO3 and (d) mesh AO4.

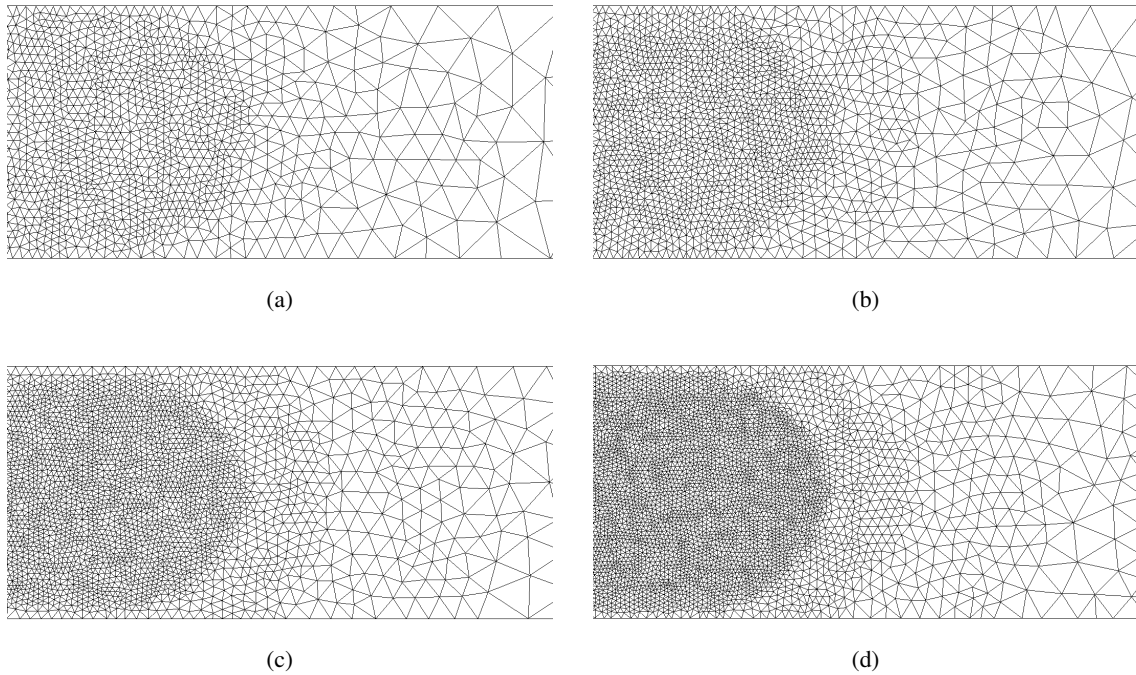


Figure 2.7: Mesh at the transition region at the downstream end of the refinement region, plane xz: (a) mesh AO1, (b) mesh AO2, (c) mesh AO3 and (d) mesh AO4.

regions of high turbulence the dissipation of heat and radicals leads to a local extinction of the flame. This would occur when the turbulence mixing timescale  $k/\varepsilon$  is smaller than a chemical timescale. An expression for the chemical timescale was also set, to avoid any situation in which the flame extinction would occur.

These three parameters (maximum flame temperature, mixing rate limit and chemical timescale) are not constant, they are functions of the mixture fraction, which corresponds to the total mass fraction of the hydrogen element in the mixture.

For the turbulent flux closure a constant value for the turbulent Schmidt number of  $Sc_{tr} = 0.7$  and the ANSYS CFX standard value for the turbulent Prandtl number are used.

## 2.3 TAU code simulations

### 2.3.1 Coaxial injector geometry

Mesh adaptations were also performed for a combustion chamber with a coaxial injector, using the TAU code. The chosen geometry is based on an experimental rocket combustion chamber studied at TU München, [20]. The chamber is a circular combustion chamber with a single element coaxial injector and a nozzle with a contraction ratio of 2.5. Since the nozzle region is out of the scope of this work, the mesh adaptation was performed only in a central region of the geometry, although the nodes and cells in the nozzle region are taken into account on the total number of nodes and

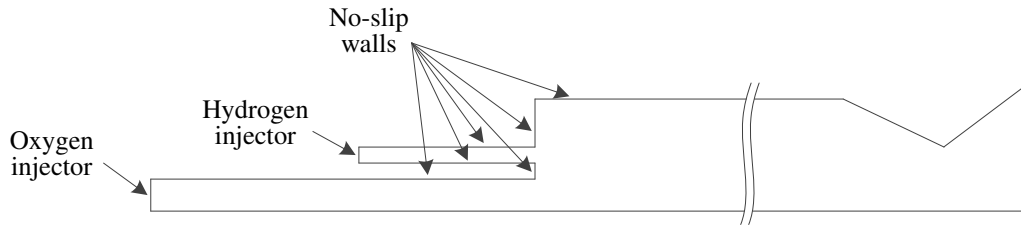


Figure 2.8: Geometry of the simulated coaxial injector.

cells for the meshes. The computational domain is a two-dimensional slice of the combustion chamber and is presented in Figure 2.8.

In this injector gaseous oxygen (GOx) is injected through the inner injector, while gaseous hydrogen (GH<sub>2</sub>) is injected by the outer one. There is no recess on the injector tips. This geometry's measures are presented in Figure 2.9 and in Table 2.4.

### 2.3.2 Coaxial injector mesh

The reference mesh for adaptation on the coaxial injector combustion chamber simulations (named TO1) is a two-dimensional axisymmetric numerical mesh created using CENTAUR software. It is composed of 80 thousands nodes 115 thousand elements, with triangular elements on the core region of the combustion chamber and quadrilateral layer inflation on the walls. The two dimension average mesh spacing of this mesh is 0.13 mm and is calculated using (2.26).

$$h = \left[ \frac{1}{N} \sum_{i=1}^N \Delta A_i \right]^{1/2} \quad (2.26)$$

Two other meshes were created for results comparison. Both were based on TO1, with an refinement region on the central area of the combustion chamber, surrounding the region where most of the combustion takes place. A summary of the meshes is presented in Table 2.5. Figure 2.10 presents examples of two regions of the meshes produced.

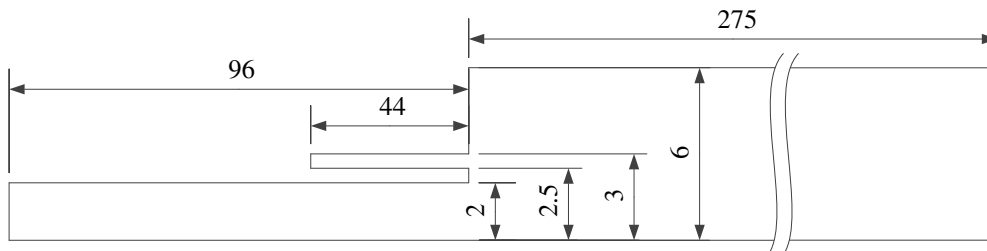


Figure 2.9: Measures of the adapted region on the coaxial injector.

Table 2.4: Summary of the coaxial injector computational domain measures.

GOx injector outer diameter	2.5 mm
GOx injector inner diameter	2 mm
GOx injector length	96 mm
GH2 injector diameter	3 mm
GH2 injector length	44 mm
Combustion chamber diameter	6 mm
Combustion chamber length	275 mm

Table 2.5: Summary of meshes used for the TAU code simulations.

Mesh	Number of nodes	Number of elements	$h$ [mm]
TO1	80 k	115 k	0.133
TO2	132 k	207 k	0.099
TO3	199 k	335 k	0.078

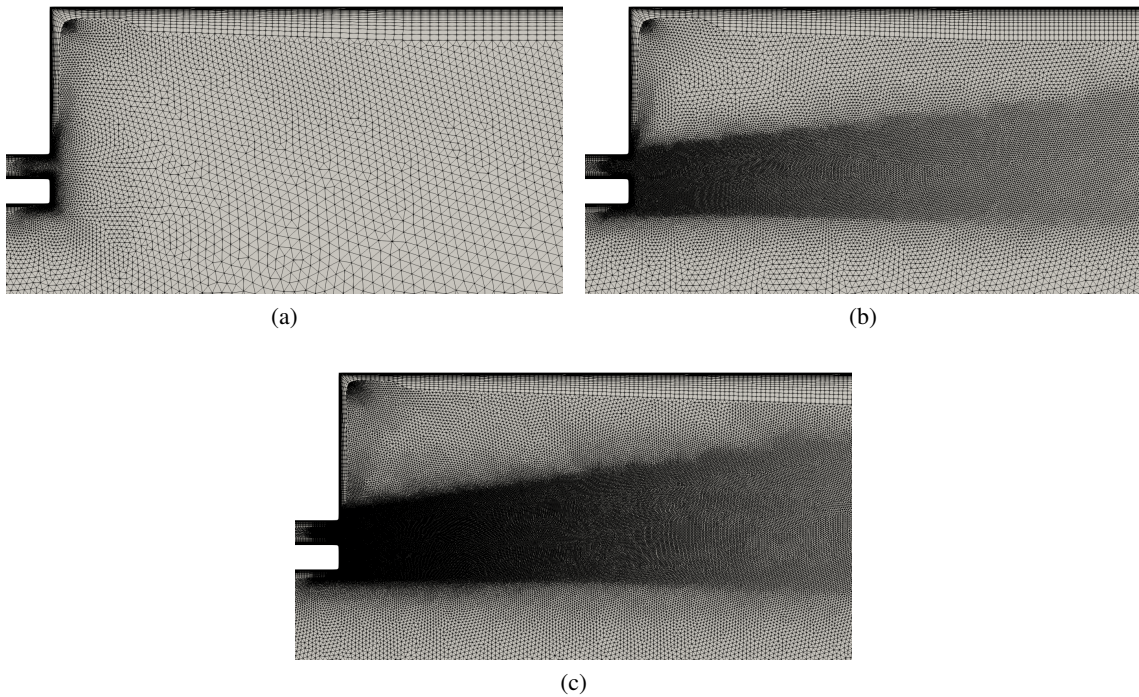


Figure 2.10: 2D mesh at the injector region: (a) mesh TO1, (b) mesh TO2, (c) mesh TO3

Table 2.6: Boundary condition for the TAU code simulations.

Injection mass flow, O <sub>2</sub>	33.9 g/s
Temperature, O <sub>2</sub>	276 K
Injection mass flow, H <sub>2</sub>	5.1 g/s
Temperature, H <sub>2</sub>	268 K
Mass ratio of oxidizer-to-fuel (ROF)	6.6
Pressure at the outlet	0.001 bar
Injector walls and faceplate temperature	300 K
Combustion chamber wall temperature	380 K
Nozzle walls temperature	500 K

### 2.3.3 TAU code simulations parameters

The coaxial injector simulations were performed using the TAU code, a CFD solver developed in-house by DLR. It is a finite volume, compressible flow solver for hybrid meshes and has been applied for a wide variety of different flows, such as steady and unsteady sub- and hypersonic applications with and without chemical reactions [17, 11, 15, 21].

The FANS equations were solved using an upwind scheme with reconstruction of gradients for second order accuracy. The turbulence was modelled using a 2-layer k- $\epsilon$  model, a model with two sets of constants, one for the flow near and the other for the flow far from the wall. The combustion is modelled using a finite rate chemistry model, with 6 species – H<sub>2</sub>, O<sub>2</sub>, H, O, HO and H<sub>2</sub>O – and 17 reactions. The values for the turbulent Schmidt and Prandtl numbers are, respectively,  $Sc_{tr} = 0.7$  and  $Pr_{tr} = 0.9$ .

The combustion chamber walls and nozzle were all no-slip walls and they were modelled assuming an one-dimensional approximation of the heat flux in a solid wall and a reservoir temperature,  $T_r$ , according to (2.27). A value of  $30000 \text{ W m}^{-2} \text{ K}^{-1}$  was set for the conduction coefficient,  $c_{cond}$ , equivalent of a copper wall 1 mm thick. The reservoir temperatures for each wall, as well as a summary of the other boundary conditions, are presented in the Table 2.6.

$$q = c_{cond} (T_w - T_r) = \lambda_w \frac{T_w - T_r}{d_w} \quad (2.27)$$

## 2.4 Mesh adaptation

Mesh adaptation is the process of modifying a mesh to accurately capture the flow features. The main idea is to improve the problem solution without excessively increasing the computational effort. There are two main mesh adaptation strategies for CFD, *r-Refinement* and *h-Refinement*. These strategies can be used alone or combined. With the r-Refinement strategy, nor the number of nodes on the mesh, nor its connectivity are changed, nodes are only moved, increasing the node density on the region of interest and decreasing it on the others. The h-Refinement strategy changes the mesh connectivity and its number of nodes, dividing cells or even adding or removing nodes, changing the mesh topology.



There are also two general methods of mesh adaptation, *incremental adaptation* and *re-meshing*. Both methods follow adaptation criteria, and while the incremental adaptation only modifies the selected nodes from the original mesh, the re-meshing does the entire geometry re-meshing every step.

### 2.4.1 ANSYS CFX mesh adaptation

For the mesh adaptation process, ANSYS CFX uses the h-Refinement strategy with an incremental adaptation method because they are simpler and faster, even if the resulting mesh quality is limited by the quality of the initial mesh [3]. ANSYS CFX mesh adaptation consist on the following steps:

1. The regions to be adapted are identified using the adaptation criteria.
2. Nodes are added to the existing mesh, according to adaptation criteria calculated.
3. The solution calculated on the previous mesh is linearly interpolated onto the new mesh.

It is possible to perform multiple adaptation steps during the same run, each one adding new nodes to the previous mesh. Nodes can also be removed during the adaptation process, but the adapted mesh can never be coarser than the original one. Only nodes that were added by previous steps of the adaptation process can be removed at later steps.

On ANSYS CFX the adaptation process is considered as a sequence of adaptation steps, starting with an initial mesh and delivering a final one. Usually, the intermediate meshes are of no particular interest. Figure 2.11 shows a schematic overview of the mesh adaptation process.

The adaptation criteria can be selected as a function of one or more variables (temperature, chemical species concentration, pressure, etc) or as a function of the variables times the edge length of the cell. Equations 2.28 and 2.29 show both possibilities, respectively. In these equations  $A_e$  is the adaptation criteria for a given mesh edge  $e$  of length  $l_e$ ,  $\phi_i$  is the  $i^{th}$  adaptation variable,  $\Delta\phi_i$  is the global range of the variable  $\phi_i$  over all nodes,  $\Delta\phi_{ei}$  is the difference between  $\phi_i$  at one end of the edge and the other end and  $N_{\phi_i}$  is a scalar for the variable  $i$  so that  $A_e$  ranges between 0 and 1. The edges with the largest adaptation criteria are marked for refinement.

$$A_e = \sum_i \frac{|\Delta\phi_{ei}|}{N_{\phi_i} |\Delta\phi_i|} \quad (2.28)$$

$$A_e = \sum_i \frac{l_e |\Delta\phi_{ei}|}{N_{\phi_i} |\Delta\phi_i|} \quad (2.29)$$

The ANSYS CFX mesh adaptation has some limitations:

- It cannot be used in multidomain nor transient simulation.
- The maximum number of node in the final mesh must be specified by the user before the run.

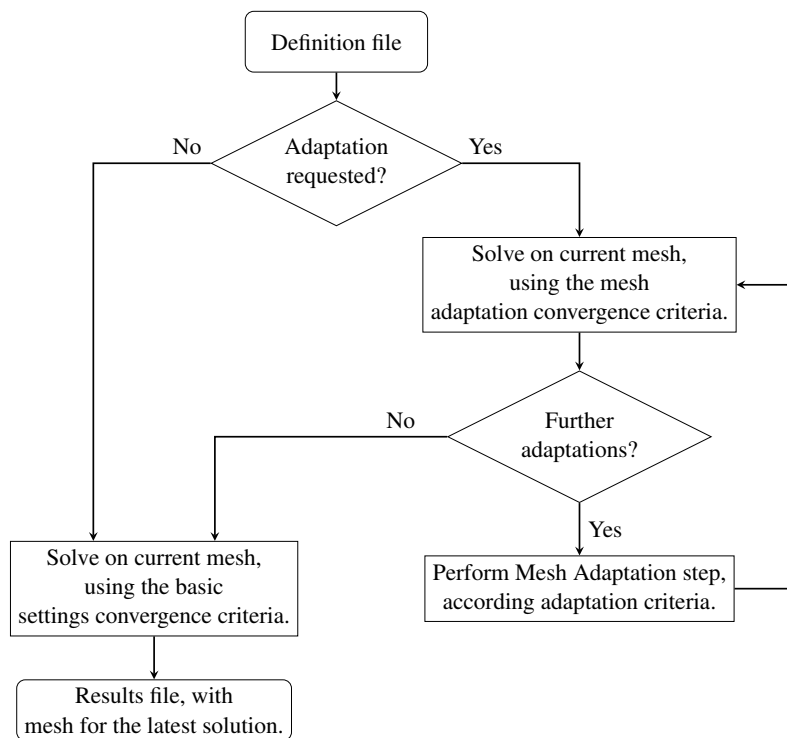


Figure 2.11: Flowchart of an ANSYS CFX mesh adaptation process. Adapted from [2]

- The method is not well-suited to meshes with high-aspect ratio elements, because it can only refine elements in a isotropic manner.
- The original mesh quality cannot be improved.

## 2.4.2 TAU code mesh adaptation

TAU code adaptation also uses an h-Refinement strategy, changing the number of nodes on the mesh, dividing elements edges. Adaptations are performed in a single step process, using as input the mesh to be adapted, a solution for this mesh, and parameters for the adaptation. Adaptation might add nodes, remove nodes or perform both actions simultaneously. There is an effort to keep the final mesh quality as close as possible from the one of the original mesh, so only certain cases of refinement on elements are allowed.

It is possible to perform adaptation on an already adapted mesh. To avoid bad quality on the mesh after several adaptation, when the new mesh is created some elements are marked as 'critical'. Refinement on these elements is not allowed, since their division might create elements with very small angles.

The basic steps of the TAU code mesh adaptation are presented bellow. Prismatic elements are treated separately since it is possible to perform adaptation only for  $y^+$  improvement.

1. Prismatic elements edges are marked to be bisected using the selected indicator and strategy. Other edges on these elements are also marked, to comply with the refinement rules.

2. Previous step is performed on tetrahedral elements.
3. Step 2 might have marked new edges on prismatic elements, so step 1 and 2 are repeated until no new additional edges are marked.
4. The new mesh is created and the 'critical' elements are marked.
5. The previous solution is interpolated on the new mesh.

Adaptation criteria is calculated for a given edge  $e$ , between points 1 and 2, by (2.30).

$$A_e = \Delta V_e \|\mathbf{x}_e\|_2^\alpha \quad (2.30)$$

where  $\Delta V_e$  is calculated by (2.31),  $\mathbf{x}_e = \mathbf{x}_{p1} - \mathbf{x}_{p2}$  and  $\alpha = 0.5$  by default.

$$\Delta V_e = \max \left( c_{\phi_i} \frac{\Delta \phi_i}{(\Delta \phi_i)_{max}} \right), \text{ with } 0 \leq i < N \quad (2.31)$$

where  $c_{\phi_i}$  is a parameters enabling to set different weights for different variables,  $\Delta \phi_i$  is a sensor value for the variable  $i$  and  $(\Delta \phi_i)_{max}$  is the maximum value of  $\Delta \phi_i$  for all edges.

There are seven sensor functions available, but for the purpose of this work, only three are considered:

- diff: differences of the variable at the nodes, (2.32).

$$\Delta \phi_i = |\phi_i(\mathbf{x}_{p1}) - \phi_i(\mathbf{x}_{p2})| \quad (2.32)$$

- grad: difference of nodes gradients, (2.33)

$$\Delta \phi_i = |\nabla \phi_i(\mathbf{x}_{p1}) - \nabla \phi_i(\mathbf{x}_{p2})| \quad (2.33)$$

- recon: reconstruction of the flow variable at the edge midface, (2.34).

$$\Delta \phi_i = \left| \left( \phi_i(\mathbf{x}_{p1}) + \frac{1}{2} \mathbf{x}_e \cdot \nabla \phi_i(\mathbf{x}_{p1}) \right) - \left( \phi_i(\mathbf{x}_{p2}) - \frac{1}{2} \mathbf{x}_e \cdot \nabla \phi_i(\mathbf{x}_{p2}) \right) \right| \quad (2.34)$$

### 2.4.3 Adaptation approach

Adaptation simulations were performed for both combustion chambers, with the API and the coaxial injector. In both cases the comparison variable for the effect of the adaptation is the distance of the flame tip from the face plate on a central line on the combustion chamber. The flame tip is considered to be the position along the oxygen injector axis where the temperature reaches 2000 K.

A list of the the parameters tested for the adaptation in both software is presented in the next sections. The parameters names are kept the same as used by the software, to allow a better usage of this work as a guide for future works using these software.

### 2.4.3.1 ANSYS CFX adaptation

The mesh adaptation of the API combustion chamber was done using ANSYS CFX and the tested parameters and their description are presented bellow. There are more parameters available on the software, but they were not focused on this work.

<i>Variable list</i>	Variables that are used for the adaptation criteria.
<i>Maximum number of steps</i>	Number of adaptation steps performed.
<i>Adaptation criteria option</i>	Control of the number of nodes on the final mesh. It can be a given number of nodes or a factor of the nodes on the initial mesh.
<i>Node factor</i>	The number of nodes on the final mesh will be the product of this number by the number of nodes on the initial mesh.
<i>Adaptation method</i>	Adaptation function to be used by the software. It can be set to use only the value of solution variables, (2.28), or to use also the edge length as input, (2.29).
<i>Maximum iterations</i>	Maximum iterations that can be performed at each adaptation step. It is only used if the convergence criteria are not met.
<i>Node allocation</i>	How much the mesh is refined at each step. When it is set to 0, the same number of nodes is added on each adaptation step, when it is positive, more nodes are added in the earlier steps and when it is negative, more nodes are added in the later steps.
<i>Number of levels</i>	Maximum number of times an edge from the original mesh can be divided.

### 2.4.3.2 TAU code adaptation

For the mesh adaptation of the coaxial injector combustion chamber the adaptation software was the one included with the TAU code. The studied parameters and their description are listed bellow. Adaptation on the boundary layer was not allowed and the weight of the total enthalpy, total pressure, density and velocity on the adaptation indicator was set to 0 (the default value is 1).

<i>Indicator type</i>	Definition of what sensor function used for determining the adaptation criteria, using diff, grad or recon.
<i>Indicator user-values</i>	List of solution variables used for the adaptation criteria.
<i>Percentage of new points</i>	Percentage of the number of nodes on the original mesh that will be added to generate the new mesh.

<i>Refinement mode</i>	Adaptation strategy, can be set to only add nodes to the grid ( <i>add</i> ), only remove nodes ( <i>remove</i> ) or perform both actions ( <i>both</i> ).
<i>h-scaling power</i>	Edge length scaling power, $\alpha$ in (2.30).



## Chapter 3

# Results and discussions

In works [25, 22, 23] a high influence of the mesh on numerical solutions of combustion chamber simulations has been observed, namely on the flame shape. The flame gets longer with an increase in the number of nodes in the mesh [23]. Therefore a mesh study for a combustion chamber with an API68 was performed. A simple solution would be to create a mesh as fine as possible to minimize the spatial discretization errors. This solution is not always possible nor efficient, due to the high computational demands, resulting in time consuming calculations. A better solution would be to refine the mesh on the critical areas, and for that the process of mesh adaptation can be a possible solution.

In this work, mesh adaptation processes have been studied, and the results from simulations have been compared, identifying the best adaptation techniques. Two different groups of adaptation were performed, one using ANSYS CFX and another using the TAU code. Since the geometry and simulations using these software are different, results were not compared between both solvers, but only within the same one, i.e. results from a given ANSYS CFX simulation were only compared with other ANSYS CFX results.

The variable used for comparison of simulations is the flame length,  $F$ , considered to be the point on a central line where  $T = 2000$  K.

### 3.1 ANSYS CFX simulations

#### 3.1.1 ANSYS CFX reference meshes

Simulations on the unadapted meshes AO1, AO2, AO3 and AO4 are used as reference for evaluation of the adapted simulations. Changes on the flame shape were observed when comparing the results of these reference meshes, the flame becomes longer and narrower with an increase in the number of nodes on the mesh. A temperature distribution along the  $x$ - $z$  base plane for these meshes is presented in Figure 3.1. This figure additionally contains a black line representing the positions of  $T = 2000$  K.

The temperature evolution on a central line passing through the oxygen injector was analysed. The temperature increase along this line was steeper for the more refined meshes. For finer meshes,

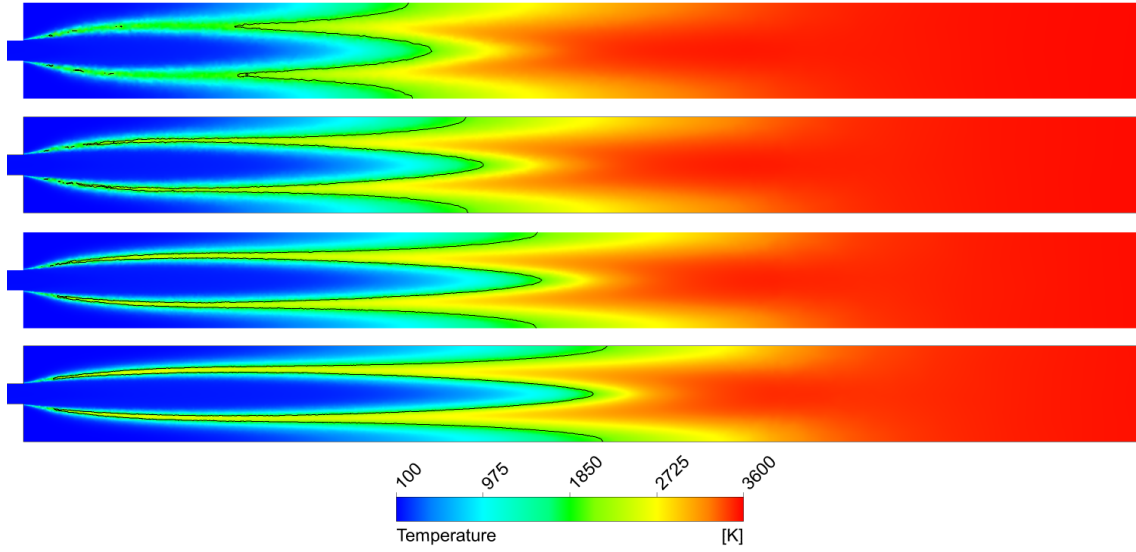


Figure 3.1: Temperature distribution on the  $x$ - $z$  base plane for the ANSYS CFX reference meshes and a black line at  $T = 2000$  K. From top to bottom, meshes AO1, AO2, AO3 and AO4.

the distance from the faceplate to the point where the temperature reaches 1000 K is longer than for the coarser meshes, however the region where the temperature goes from 1000 K to 3000 K is shorter. This behaviour of the temperature change is shown in Figure 3.2, for distances between 15 mm and 55 mm from the faceplate.

The flame length for the meshes AO1, AO2, AO3 and AO4 was determined, and the increase on the flame length,  $F_{i,A}$ , compared to the mesh AO1 was calculated by (3.1). The values for  $F$  and  $F_{i,A}$  for the reference meshes are given in the Table 3.1. The flame lengths of the reference meshes were fitted using a second order curve, based on the average mesh spacing  $h$  defined by (2.24). The curve fit is present in the Figure 3.3. With this curve fit it was possible to calculate a value of the reference flame length for any given mesh spacing, and so this curve will be used for further evaluation of the adapted meshes. From the curve fit, the calculated flame length for  $h = 0$  is 54.82 mm.

$$F_{i,A} = \frac{F_i - F_{AO1}}{F_{AO1}} \quad (3.1)$$

Variables were also analysed along a line at the base plane  $x$ - $z$ , located at  $x = 15$  mm from the

Table 3.1: Summary of flame length for ANSYS CFX reference meshes.

Mesh	$F$ [mm]	$F_{i,A}$ [%]
AO1	30.15	-
AO2	33.98	12.72
AO3	38.27	26.94
AO4	42.1	39.64



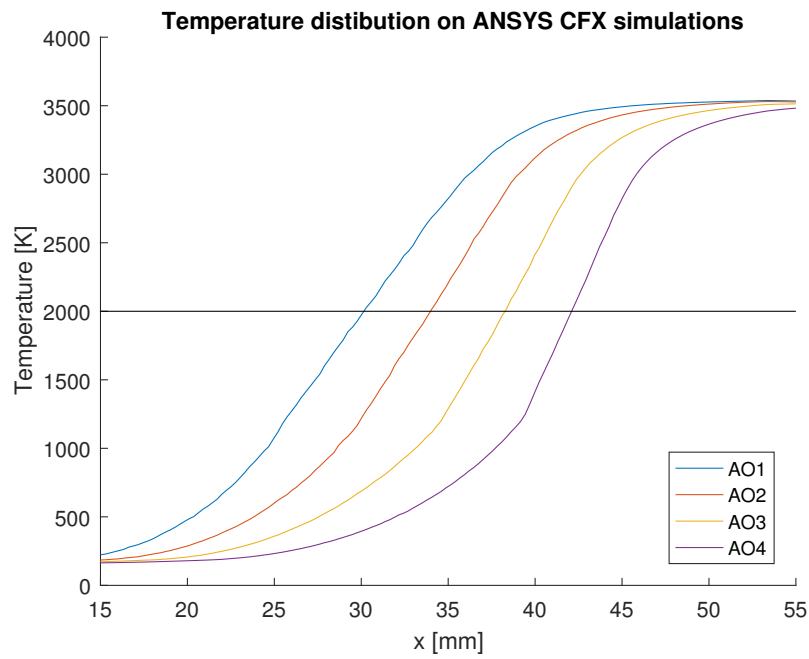


Figure 3.2: Temperature distribution along a central line for the ANSYS CFX reference meshes simulations.

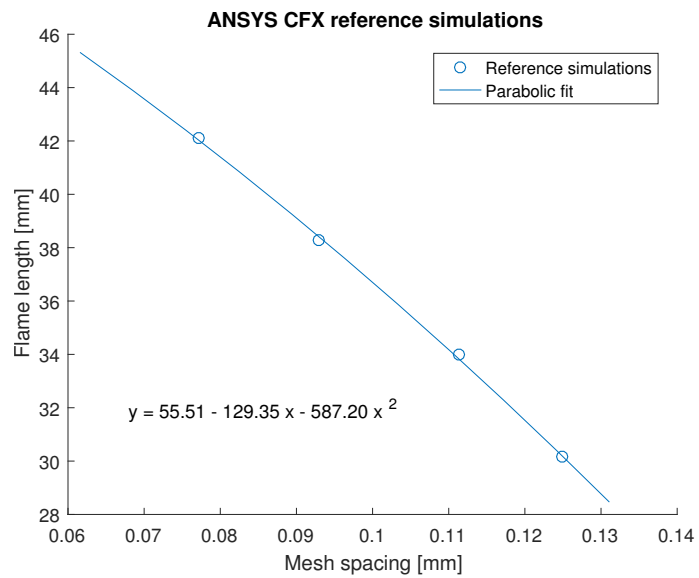


Figure 3.3: ANSYS CFX reference curve fit for flame length.

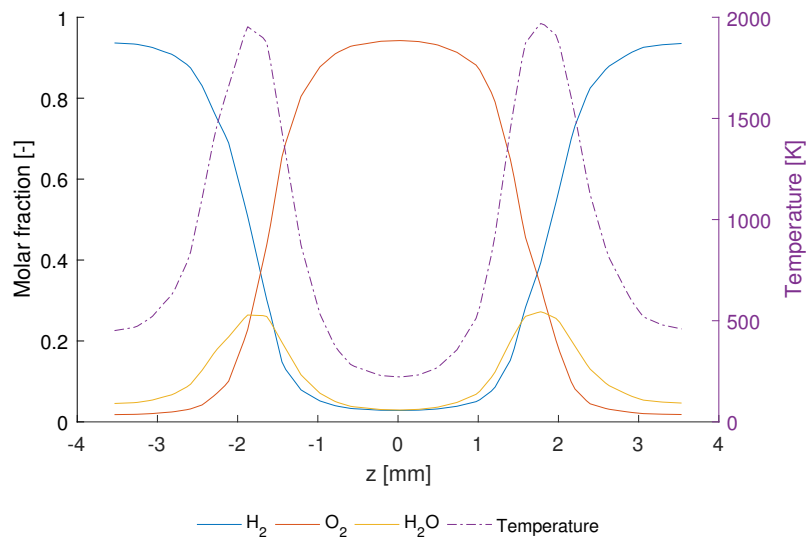


Figure 3.4: Radial evolution of temperature, H<sub>2</sub>, O<sub>2</sub> and H<sub>2</sub>O molar fractions along a line parallel to the faceplate, distant 15 mm, for the AO1 mesh.

faceplate and parallel to it. The molar fraction of H<sub>2</sub>, O<sub>2</sub> and H<sub>2</sub>O, as well the temperature on this line are presented in Figure 3.4. One can see the regions of highest reaction rate in this line. These regions are where the temperature and H<sub>2</sub>O mass fraction reach their highest values and they are the same regions where the mass fractions of H<sub>2</sub> and O<sub>2</sub> have similar values.

Due to the geometry of the injector, with the O<sub>2</sub> injector on the centre, the molar fraction of oxygen has the highest value in the centre, near  $z=0$  mm. This value is close to one, showing that hydrogen and water molecules diffuse to the oxygen core. Hydrogen is uniformly injected through the face plate of the injector, but its molar fraction is higher near the symmetry boundaries, due to the reaction with the oxygen. These distributions of molar fractions and temperature are important to understand the results from the mesh adaptation processes in next sections.

### 3.1.2 ANSYS CFX mesh adaptation parameters

Simulations were made with different combinations of parameters, aiming to isolate the influence of each parameter on the adapted mesh solution. Different adaptation strategies were tested, smoothing the meshes and performing dynamical adaptation simulations. These strategies will be explained in sections 3.1.2.1 and 3.1.2.2. A list of used values for these adaptation parameters is shown in the Table 3.2 and the complete list of adaptations simulations performed is available in the Appendix A.

From here on, all ANSYS CFX simulations will be referenced by their name as presented in Appendix A. The names of the simulations are based on the variables select for the adaptation criteria and the number of simulations already performed with these same variables. For example, A\_T.H2O\_03 is the third ANSYS CFX (A) adaptation simulation using temperature (T) and H<sub>2</sub>O molar fraction (H2O) as adaptation variables. Special cases, like the smoothing strategies and the dynamical adaptations, are also noted on the names of the simulations.

Table 3.2: Tested values for ANSYS CFX adaptation parameters.

Parameter	Tested values
Variable list	Temperature
	H <sub>2</sub> O molar fraction
	O <sub>2</sub> molar fraction
	H <sub>2</sub> molar fraction
	Density
	Velocity
	Static entropy
	Eddy viscosity
	Total enthalpy
	Vorticity
	Hydrogen-Oxygen Reaction Rate
Radial Velocity ( $V_{vw} = \sqrt{v^2 + w^2}$ )	
Maximum number of steps	5 to 1000
Adaptation criteria option	Multiple
Node factor	3
	4
Adaptation method	Solution variable
	Solution variable $\times$ Length
Maximum iterations	1 to 1000
Node allocation	0 to 10
Number of levels	1 to 3

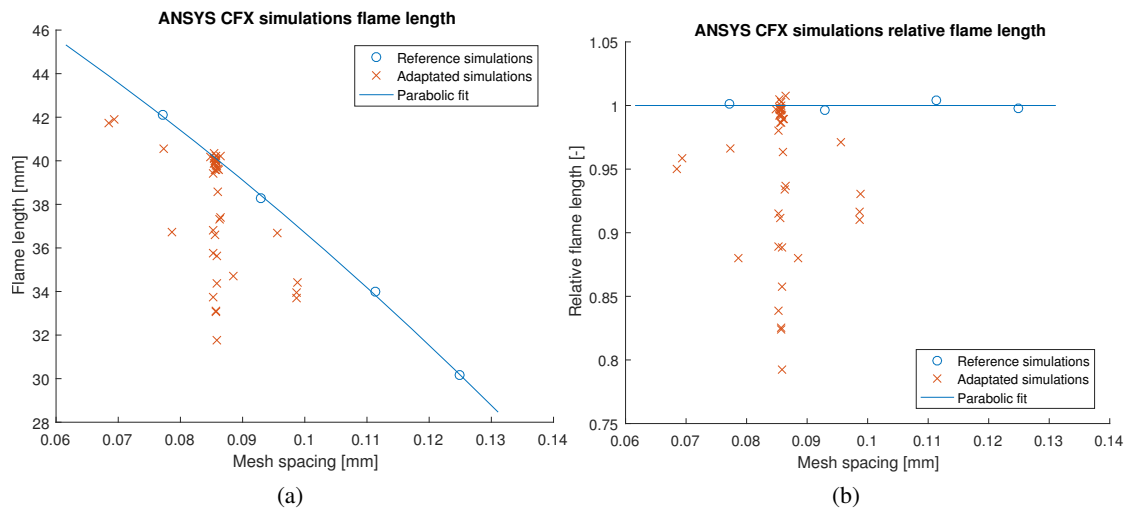


Figure 3.5: Flame length for ANSYS CFX simulations compared to the reference curve: (a) absolute values, (b) relative values.

For the simulations, all adaptation parameters were locked, and only one parameter value was changed at a time, verifying the influence of different values of this parameter on the final solution. The flame length and mesh spacing of every simulation were determined, and using the mesh spacing and the reference curve fit, a reference flame length was calculated. Figure 3.5a shows the flame lengths for all the simulations. For a better visualization of the impact of the adaptation on the flame length, a relative flame length,  $F_{rel}$ , was calculated dividing the simulated flame length by the reference one, as presented in Figure 3.5b. The larger the value of the relative flame length,  $F_{rel}$ , the better the solution. Simulations for each parameters were compared, and the best value for each parameter was determined.

The best values for the parameter "variable list" are combinations of temperature and the species molar fractions. These variables are directly related to the combustion process, and their variations are also interrelated, as shown in the Figure 3.4. Simulations using only temperature as adaptation variable presented good results, but the combination of this variable with additional parameters improved the solution even more. The temperature has regions of high gradient in both sides of the flame, visible in Figure 3.4. More refinement will occur in these regions, since, on mesh adaptation, edge splitting occurs where the differences of a variable along the edge are larger, that is, where the variable gradients are larger. Combining temperature with other combustion related variables provides more information to the adaptation algorithm, leading to an improved solution. Different combinations of temperature and the species molar fractions have different results, but the difference between them is below 1%. The relative flame length for different values of the adaptation parameter "variable list" is presented in the Figure 3.6.

The parameter "adaptation method" can only assume two different values, and so three pairs of simulations were performed. For these sets, other parameter were also changed, verifying the influence of "adaptation method" in different configurations. A summary of these simulations is presented in the Table 3.3. Longer flames were obtained when this parameter was set to "Solution

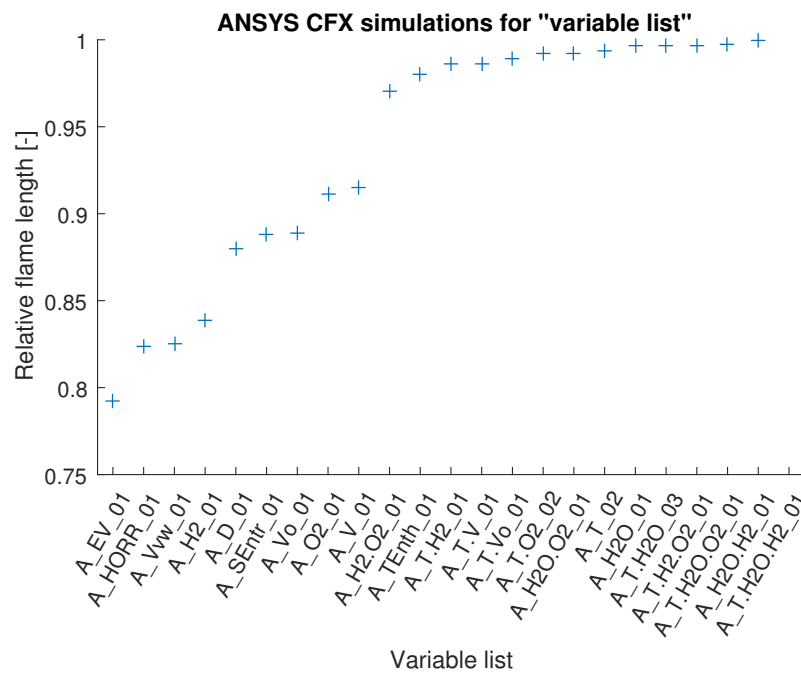


Figure 3.6: Comparison of  $F_{rel}$  for different values of "variable list".

variable  $\times$  Length", as presented in the Figure 3.7. When ANSYS CFX considers the edge length into the calculation of the adaptation criteria, fewer short edges are split, decreasing the creation of elements with bad quality, this way producing meshes with better quality.

Two sets of simulations were performed to verify the influence of the adaptation parameter "node allocation" on the final mesh and they are presented in the Table 3.4. Only positive values of this parameter were tested, that is, more nodes were added during the initial steps of the adaptation process. During the mesh adaptation there is an iterative process of refining the mesh and changes on the flame. Adding more nodes at the initial step allows these nodes to be reallocated at later steps, tracking the flame as it changes. Adding too many nodes during initial steps could also lead to instabilities on the solution, since it causes larger changes on the mesh at each step. The number of nodes added per step depends also on the adaptation total number of steps. For an "maximum number of steps" of 5, approximately 44% of the new nodes are added on the first step for "node allocation" equals 1, 68% for "node allocation" equals 2 and 84% for 3. The best values for "node allocation" were different for the two sets of simulations, but since simulation A\_T.H2O\_14 did not have a good residual convergence, its results were not considered as best one, and then best value for this parameter was 2. The results of the tests for this parameter are presented in the Figure 3.8. The best value found for "node allocation" is in accordance with the ANSYS CFX Pre-User's Guide [2], that recommends values between -2 and 2 for this parameter.

For the simulation parameter "number of levels", two set of simulations were performed and are presented in the Table 3.5. The best value for this parameter is 1. Values larger than 2 were not tested, since it was verified that splitting the edges more than once resulted in a smaller relative flame length. This parameter also affects the mesh quality, since more than one splitting per

Table 3.3: Parameters of the simulation for "adaptation method" tests.

Set	Simulation	Variable list	Adap. method	Node alloc.	Num. of levels	$F_{rel}$
1	A_T.H2O_03	temperature, H <sub>2</sub> O molar fraction	var×len	1	1	0.9965
	A_T.H2O_06	temperature, H <sub>2</sub> O molar fraction	var	1	1	0.9893
2	A_T.H2O_08	temperature, H <sub>2</sub> O molar fraction	var×len	1	2	0.9337
	A_T.H2O_07	temperature, H <sub>2</sub> O molar fraction	var	1	2	0.8573
3	A_T.H2O_09	temperature, H <sub>2</sub> O molar fraction	var×len	2	1	0.9972
	A_T.H2O_10	temperature, H <sub>2</sub> O molar fraction	var	2	1	0.9918

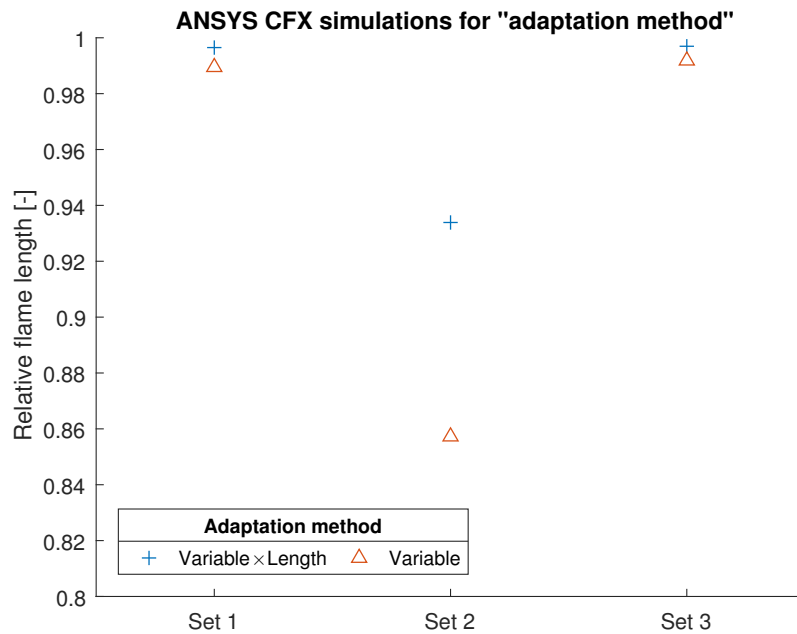
Figure 3.7: Comparison of  $F_{rel}$  for different values of "adaptation method".

Table 3.4: Parameters of the simulations for "node allocation" tests.

Set	Simulation	Variable list	Adap. method	Node alloc.	Num. of levels	$F_{rel}$
1	A_T.H2O_03	temperature, H <sub>2</sub> O molar fraction	var×len	1	1	0.9965
	A_T.H2O_09	temperature, H <sub>2</sub> O molar fraction	var×len	2	1	0.9972
	A_T.H2O_13	temperature, H <sub>2</sub> O molar fraction	var×len	3	1	0.9968
2	A_T.H2O_06	temperature, H <sub>2</sub> O molar fraction	var	1	1	0.9893
	A_T.H2O_10	temperature, H <sub>2</sub> O molar fraction	var	2	1	0.9918
	A_T.H2O_14	temperature, H <sub>2</sub> O molar fraction	var	3	1	0.9946

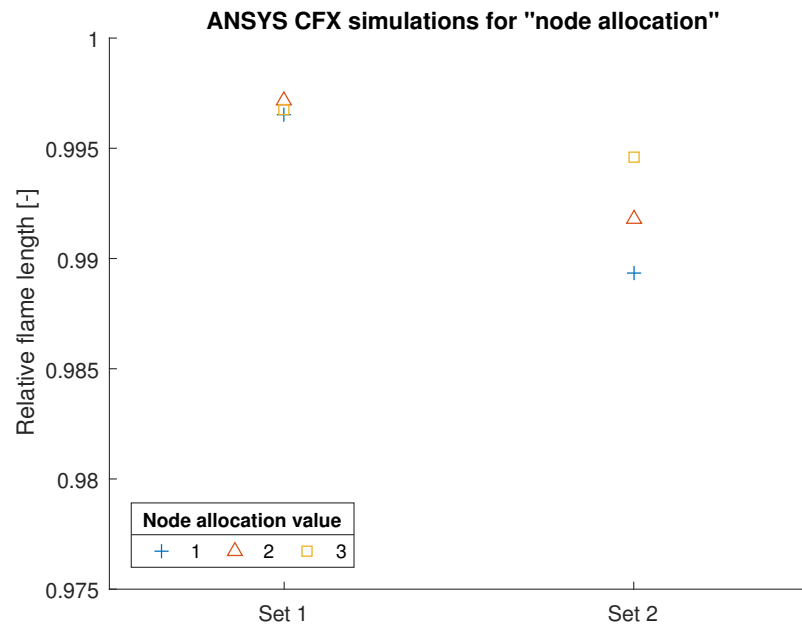
Figure 3.8: Comparison of  $F_{rel}$  for different values of "node allocation".

Table 3.5: Parameters of the simulations for "number of levels" tests.

Set	Simulation	Variable list	Node factor	Adap. method	Node alloc.	Num. of levels	$F_{rel}$
1	A_T.H2O_03	temperature, H <sub>2</sub> O molar fraction	3	var×len	1	1	0.9965
	A_T.H2O_08	temperature, H <sub>2</sub> O molar fraction	3	var×len	1	2	0.9337
2	A_T.H2O_06	temperature, H <sub>2</sub> O molar fraction	3	var	1	1	0.9893
	A_T.H2O_07	temperature, H <sub>2</sub> O molar fraction	3	var	1	2	0.8573

original edge may lead to bigger differences on the size of neighbours elements, producing meshes with lower quality. Figure 3.9 shows all simulation results for "number of levels" tests.

Some best values were chosen based not only on the calculated relative flame length. For example, the value of "maximum number of steps" was set to five, following the recommendation of the ANSYS CFX Pre-User's Guide [2]. Higher values of the relative flame length were obtained for higher values of "maximum number of steps", as presented in Table 3.6, but this increase was not worth the longer time demanded for the simulation. A summary of the best values for the parameters is presented in the Table 3.7.

It is noticeable that some parameters have more influence on the final solution than others. For example, the values of the relative flame length varied less than 0.5% in the simulations for "node allocation", while they varied more than 20% in the "variable list" tests.

Other strategies were also tested, such as smoothing the adapted mesh and running dynamical adaptations, with several steps in unconverged solutions.

### 3.1.2.1 ANSYS CFX smoothing strategy

An approach tried was to perform a mesh smoothing on ANSYS ICEM CFD after the adaptation process, to increase the mesh quality. In general, the adapted meshes generate by the ANSYS CFX adaptation process have lower quality than the original mesh, with several low quality elements.

Table 3.6: Parameters of the simulations for "maximum number of steps" tests.

Simulation	Variable list	Max. num. steps	Adap. method	Node alloc.	Num. of levels	$F_{rel}$
A_T.H2O_03	temperature, H <sub>2</sub> O molar fraction	5	var×len	1	1	0.9965
A_T.H2O_05	temperature, H <sub>2</sub> O molar fraction	10	var×len	1	1	0.9981



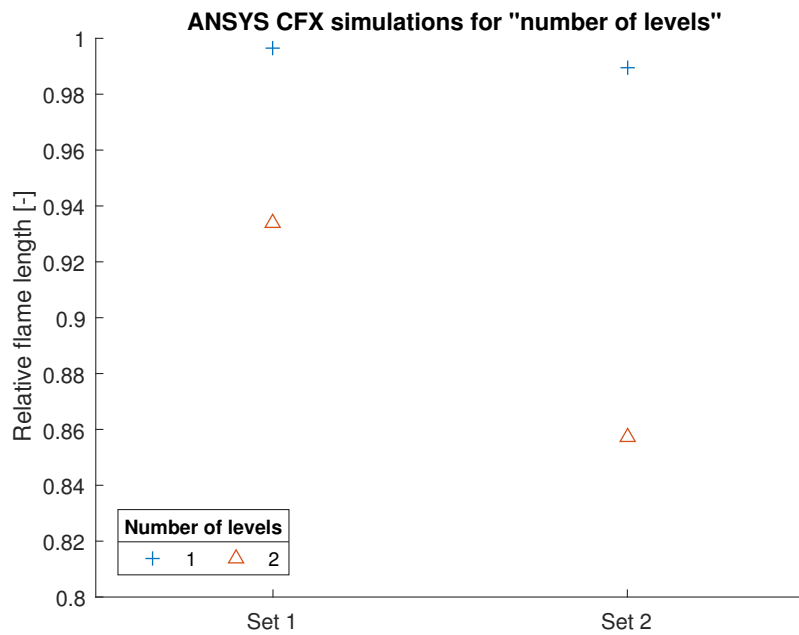


Figure 3.9: Comparison of  $F_{rel}$  for different values of "number of levels".

Table 3.7: Best values for ANSYS CFX adaptation parameters.

Parameter	Best value
Variable list	Temperature, H <sub>2</sub> O Molar Fraction and H <sub>2</sub> Molar Fraction H <sub>2</sub> O Molar Fraction and H <sub>2</sub> Molar Fraction Temperature, H <sub>2</sub> O Molar Fraction and O <sub>2</sub> Molar Fraction Temperature, H <sub>2</sub> Molar Fraction and O <sub>2</sub> Molar Fraction Temperature and H <sub>2</sub> O Molar Fraction H <sub>2</sub> O Molar Fraction Temperature H <sub>2</sub> O Molar Fraction and O <sub>2</sub> Molar Fraction Temperature, O <sub>2</sub> Molar Fraction
Maximum number of step	5
Adaptation method	Solution variable × Length
Node allocation parameter	2
Number of levels	1

These bad quality elements appear because ANSYS CFX marks the edges to be split based only on the adaptation criteria, it does not consider the elements shape nor their angles before splitting the edges.

The smoothing process moved some mesh nodes and merged others, eliminating the low quality elements. This higher quality mesh improved the final solution, increasing the flame length. Smoothing the mesh between every adaptation step could be a good strategy, but it would demand more effort and working time from the users, something opposite to the objective of this work.

Besides demanding more from the user, smoothing between every adaptation might not have good results with the ANSYS CFX adaptation algorithm. During adaptation, ANSYS CFX is not allowed to coarsen the edges of the original mesh. Smoothing the mesh between each adaptation step would make the new adaptation to be performed on an "original mesh", so nodes would only be added, not moved. Doing so, the adaptation process loses its capacity of tracking the flame.

Despite showing relative good results, with a relative flame length up to 1.008, this strategy was not extensively tested, since it was considered to be out of the scope of this work.

### 3.1.2.2 ANSYS CFX dynamical adaptation strategy

Another tested strategy for the mesh adaptation was the dynamical adaptation, running adaptations with hundreds of steps, before a solution convergence on the mesh. After each adaptation step, only a few iterations were done, between 1 to 50, and then a new adaptation was performed. There was no solution convergence before the mesh adaptation process. It was expected that adapting the mesh after only small changes on the results would lead to small changes on the resulting mesh, and then mesh and solution would converge together to a conjunct result.

Results were not as expected and the solution did not converge. Adapting the mesh before the convergence of the solution created an unstable flame, that would keep changing its length, getting longer and shorter when changing the mesh. The refinement of the region near the faceplate has an important effect on the flame length, and adapting mesh with a shorter flame, makes new elements to be added next to the faceplate, increasing the flame length. Adapting a longer flame mesh causes nodes near the faceplate to be moved further downstream, decreasing the flame length. With a shorter flame, the mesh adaptation moves nodes back to the faceplate, increasing the flame length and repeating the cycle. This process continues and no convergence is obtained. This strategy was considered not successful.

### 3.1.3 ANSYS CFX simulation results

A simulation, named A\_T.H2O.H2\_02, was performed with all parameters set to its best values. The flame lengths of all adaptation simulation were compared to the second order curve fit for the reference simulations, and the simulations with largest and smallest relative flame length are presented in the Figure 3.10. Details of the results of this simulations are presented in the Table 3.8.

The largest value obtained for  $F_{rel}$  was for the simulation A\_S\_T.H2O\_03\_01, a simulation with mesh smoothing. Since the smoothing strategy was not considered desirable for this work,

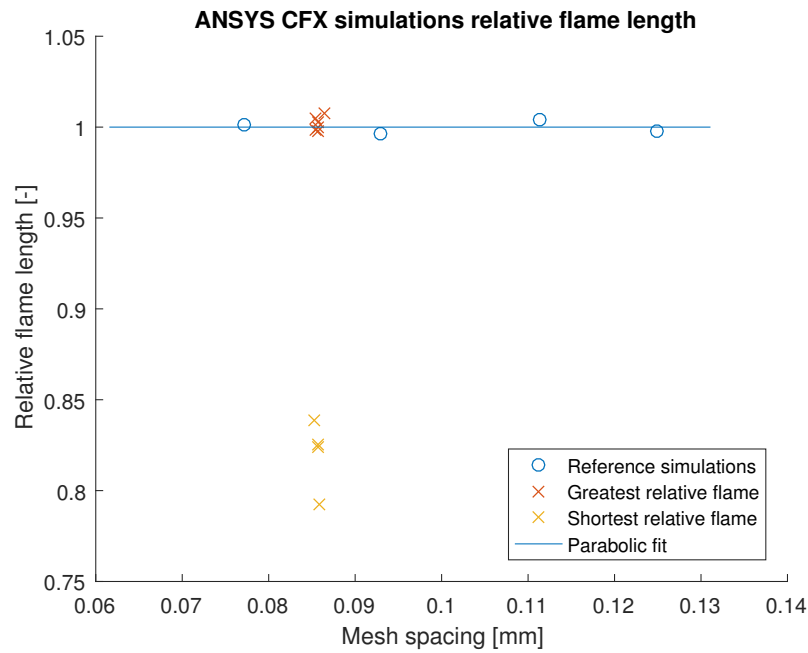


Figure 3.10: ANSYS CFX simulations with the largest and smallest reference flame length.

Table 3.8: ANSYS CFX adaptation simulations with the largest and smallest relative flame lengths.

Simulation	Number of nodes	Number of elements	$F_{rel}$	$F$ [mm]	$F_{i,A}$ [%]	$h$ [mm]
AO1	300 k	1.45 M	0.998	30.15	-	0.125
AO2	385 k	2.05 M	1.004	33.98	12.72	0.111
AO3	651 k	3.51 M	0.996	38.27	26.94	0.093
AO4	1.13 M	6.16 M	1.001	42.1	39.64	0.077
A_S_T.H2O_03_01	844 k	4.362 M	1.037	40.24	33.46	0.087
A_T.H2O.H2_02	900 k	4.518 M	1.004	40.35	33.87	0.085
A_T.H2O.H2_01	892 k	4.475 M	1.002	40.21	33.37	0.086
A_H2O.H2_01	892 k	4.473 M	0.999	40.09	32.99	0.086
A_T.H2O_05	898 k	4.536 M	0.999	40.12	33.07	0.085
A_T.H2O.O2_01	892 k	4.474 M	0.998	40.00	32.69	0.086
		...				
A_H2_01	898 k	4.564 M	0.838	33.73	11.90	0.085
A_Vvw_01	892 k	4.484 M	0.825	33.11	9.81	0.086
A_HORR_01	892 k	4.493 M	0.824	33.06	9.67	0.086
A_EV_01	879 k	4.460 M	0.793	31.77	5.38	0.086

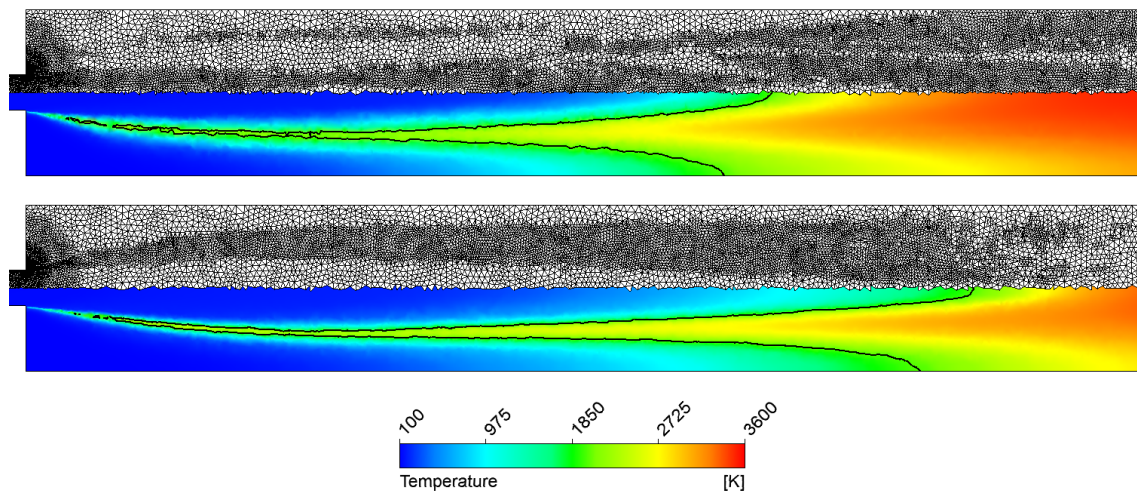


Figure 3.11: Temperature distribution, a line of  $T = 2000$  K and the mesh of the simulations A\_EV\_01 (top) and A\_T.H2O.H2\_02 (bottom).

the simulation A\_T.H2O.H2\_02 was considered as the best simulation for further analysis. The simulation A\_EV\_01 was considered the worst one. A comparison of the temperature distribution and the mesh of these two simulations is presented in the Figure 3.11. It is noticeable the mesh refinement on the surrounding of  $T = 2000$  K on the simulation A\_T.H2O.H2\_02. On the the simulation A\_EV\_01 the refinement regions are not related to regions of chemical reaction but mainly to the inner part of the oxygen jet. Therefore, the flame length was not much improved. This comparison shows that the setting of parameters plays a major role on the adapted regions and, by consequence, on the final flame length.

The temperature evolution along a central line for the A\_S\_T.H2O\_03\_01 and A\_EV\_01 simulations was compared to those from the ANSYS CFX reference simulations. It was observed that the temperature evolution behaviour on the adapted meshes was different than that on the reference meshes. The temperature curves of the reference meshes, in Figure 3.2, have all similar shapes, with three visually distinguishable regions, with boundaries near  $T = 1000$  K and  $T = 3000$  K. For the adapted meshes the temperature curves have different shapes and do not fit in the same regions divisions. Simulations A\_EV\_01 and A\_S\_T.H2O\_03\_01 have similar values of the temperature until near  $x = 25$  mm, but from that point further the temperature evolution for these simulations differ, with A\_EV\_01 presenting a steeper increase in the temperature than A\_S\_T.H2O\_03\_01. These changes show the influence of the mesh refinement on the temperature evolution on the simulations.

### 3.1.4 ANSYS CFX simulations conclusions

It was observed that ANSYS CFX was capable of adapting the mesh for combustion simulations. The mesh adaptation process has a great dependence of the simulations parameters and some parameters have stronger influence on the adaptation process than others. The relative flame length

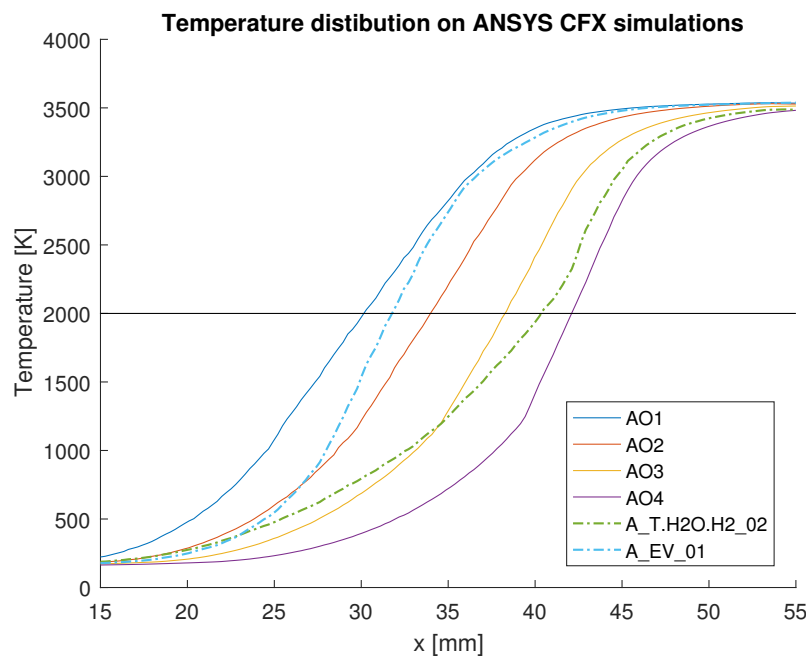


Figure 3.12: Temperature distribution along a central line for the best, worst and reference ANSYS CFX simulations.

of the "variable list" test simulations had larger variation in value than those of "node allocation parameter", for example. Different combinations of values for "variable list" could also generate different solutions, but they were not tested.

Simulations were made to determine the best values for the ANSYS CFX simulations parameters, and they are presented in the Table 3.7. The simulations were analysed using a relative flame length, based on the flame length of the simulation and a reference flame length, defined by the flame length of the reference meshes. The largest relative flame length obtained was 1.037 and the worst was 0.793. Other strategies were also tested. Smoothing the mesh after adaptation showed to improve the solution, but it demands time and effort from the user and was considered out of the scope of this work. Dynamical adaptations, with several adaptation steps applied to unconverged solutions, were not successful for ANSYS CFX and no convergence was obtained.

For the studied case, ANSYS CFX mesh adaptation increased the flame length, but the obtained results were below or too close to the reference values, that is, similar or better results could be obtained by directly refining the mesh, refining it without any adaptation process. The computational time demanded for the ANSYS CFX mesh adaptation of the studied case does not justify the obtained results.

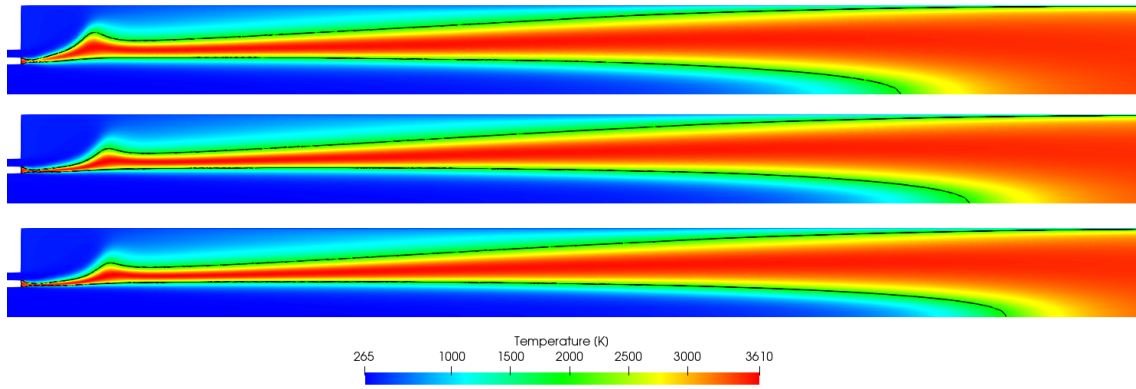


Figure 3.13: Temperature distribution for the TAU code reference meshes and a black line at  $T=2000$  K. From top to bottom, TO1, TO2, TO3. The axial direction is clinched by a factor of 2.

## 3.2 TAU code simulations

### 3.2.1 TAU code reference meshes

For the TAU code mesh adaptation studies the meshes TO1, TO2 and TO3 were used as reference meshes. Similar to the ANSYS CFX simulations, refining the meshes changed the shape of the flame, getting longer as the mesh was refined. The temperature distributions for the three TAU code reference meshes are shown Figure 3.13. In this figure there is a black line representing the positions of  $T = 2000$  K. There is a recirculation after the injector faceplate, creating a bump on the flame. Near to the faceplate the flame gets wider and then thinner in a short distance. The bump gets thinner and move forward with the mesh refinement.

The temperature distribution was also analysed along the geometry symmetry axis, presented in Figure 3.14 for a region between 80 mm and 170 mm. Similar to what was observed on the ANSYS CFX reference simulations, the temperature increase is steeper for the more refined meshes. The temperature curves can be divided in three regions with different behaviours, a region with an increase in temperature variation, before  $T \approx 1500$  K, an almost linear region between  $T \approx 1500$  K and  $T \approx 2500$  K, and a region of decrease in the temperature variation, after  $T \approx 2500$  K.

The flame length for the TAU code reference meshes was calculated and the increase on the flame length,  $F_{i,T}$ , was calculated by (3.2). The values for the flame length and the increase in the flame length for the reference meshes is presented in the Table 3.9. Similar to the ANSYS CFX reference meshes analysis, the flame lengths of the reference meshes were fitted using a second order curve, using the mesh spacing  $h$  as argument, creating a reference flame length for any given mesh spacing. The curve fit for the TAU code reference flame length is presented in the Figure 3.15.

$$F_{i,T} = \frac{F_i - F_{TO1}}{F_{TO1}} \quad (3.2)$$

The temperature and the mass fraction of the species were analysed along a radial line located at  $x = 60$  mm from the faceplate. The mass fraction of  $H_2$ ,  $O_2$ ,  $H_2O$ ,  $H$ ,  $O$  and  $H$ , as well as

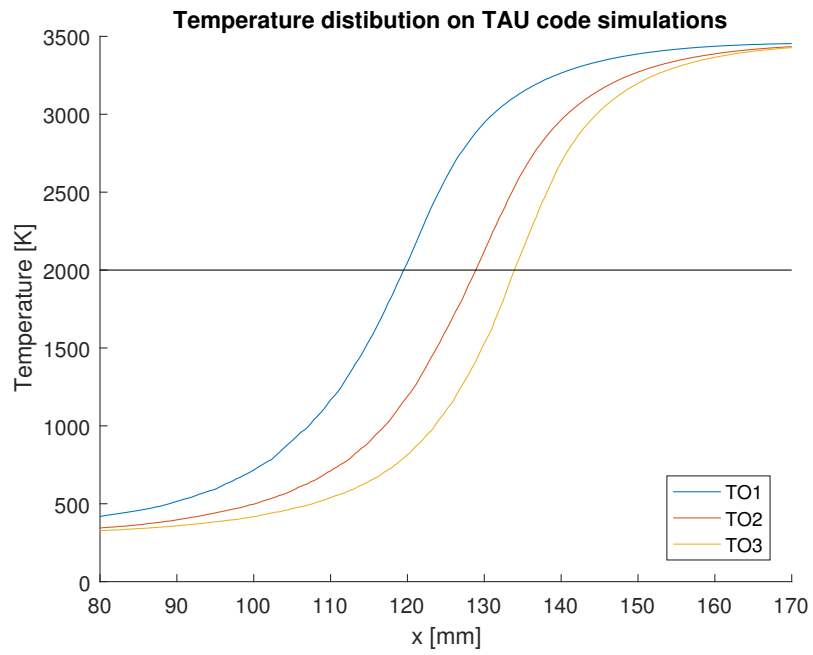


Figure 3.14: Temperature distribution along a central line for the TAU code reference meshes simulations.

Table 3.9: Summary of flame length for TAU code reference meshes.

<b>Mesh</b>	<b><math>F</math> [mm]</b>	<b><math>F_{i,T}</math> [%]</b>
TO1	119.51	-
TO2	128.89	7.85
TO3	133.91	12.05

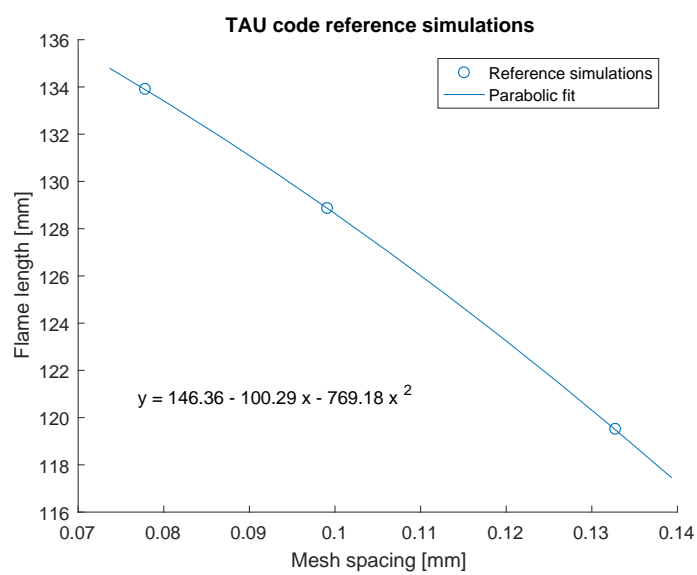


Figure 3.15: TAU code reference curve fit for flame length.

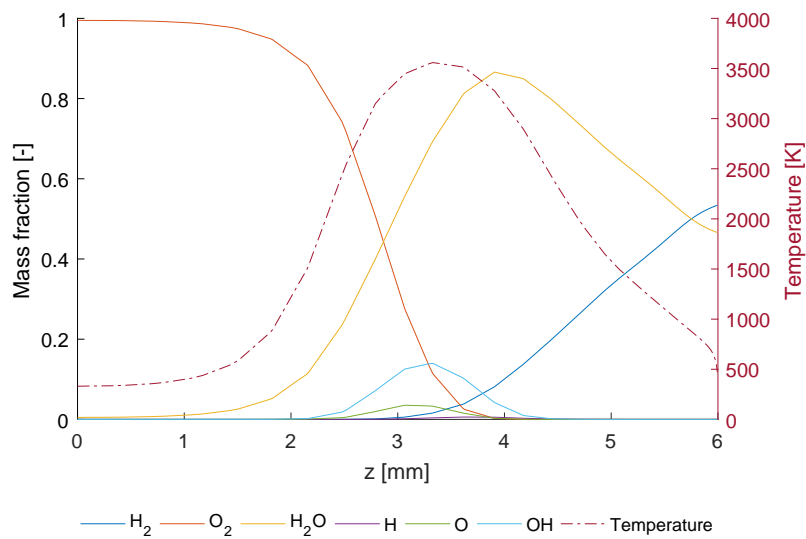


Figure 3.16: Radial evolution of temperature and species mass fractions along a line parallel to the faceplate, distant 60 mm, for the TO1 mesh.

the temperature along this line are presented in the Figure 3.16. In these curves it is possible to distinguish the region of highest reaction rates, where the temperature, the OH and O mass fractions reach their highest values. This is the same region where the mass fractions of H<sub>2</sub> and O<sub>2</sub> have similar values.

The oxygen injection, through the centre of the faceplate, creates an oxygen core, with a mass fraction of O<sub>2</sub> close to one near the centre line, at  $z=0$  mm. Others species diffuse to the oxygen core, decreasing the value of O<sub>2</sub> mass fraction in the radial direction. Near the walls, at  $z=6$  mm, the temperature has a abrupt decrease, due to heat flux through the walls. This decrease in temperature also causes the formation of water near the wall, what can be observed by a higher H<sub>2</sub>O mass fraction near the wall, when compared to the value at the centre line.

### 3.2.2 TAU code mesh adaptation parameters

Similar to the strategy used for the ANSYS CFX simulations, the TAU code adaptations were made with different combinations of parameters to identify the influence of each one on the adapted mesh solution. The dynamical adaptation strategy was also tested for the TAU code adaptation. A list of the values used for adaptation parameters is presented in the Table 3.10, and the complete list of adaptation simulation using the TAU code is presented in the Appendix B. The explanation of the adaptation parameter is presented in the section 2.4.3.1. The TAU code gives the user more control over each adaptation step, since every adaptation process can be considered as a single step and the number of new nodes to be added to the mesh can be defined per step. Different combinations of "percentage of new points" and the number of steps were tested. They are represented in the Table 3.10 as "number of steps  $\times$  percentage of new points" on the row "percentage of new nodes".



Table 3.10: Tested values for TAU code mesh adaptation.

Parameter	Tested values
Indicator user-values	Temperature
	H <sub>2</sub> mass fraction
	O <sub>2</sub> mass fraction
	H mass fraction
	O mass fraction
	OH mass fraction
	H <sub>2</sub> O mass fraction
Indicator type	diff
	grad
	recon
h-scaling power	0
	0.5
	1
Percentage of new points	1×25
	2×25
	3×25
	4×25
	5×25
	1×75
	1×75 + 1×5
	1×75 + 2×5
	10×7 + 190×0
10×7 + 290×0	
Refinement mode	both

The TAU code simulation names presented in Appendix B are based on the parameter values used for the simulations, when these values are different from the default. For example, the simulation T\_T\_diff\_1s is TAU code simulation (T), using temperature (T) as adaptation variable, "diff" as indicator type and one adaptation step (1s). The simulation T\_T\_recon\_a1\_75.5.5\_3s is a TAU code simulation (T) that uses temperature (T) as adaptation variable, "recon" as indicator type, considers the "h-scaling power" –  $\alpha$  in (2.30) – as 1 (a1) and was performed in three steps (3s) adding 75% of new nodes on the first step and 5% on the second and third steps. The dynamical simulations are named based on the number of iterations per step, for example, T\_T\_diff\_100i\_200s is a dynamical simulation with 200 steps (200s) and each of them had 100 iterations (100i).

The simulations for parameter testing with the TAU code were made in a similar way as the ANSYS CFX simulations, locking all parameters and changing only one at a time, in order to verify the influence of this parameter on the final solution. The obtained mesh spacing and the obtained flame length for every solution were calculated and then compared to the values on the

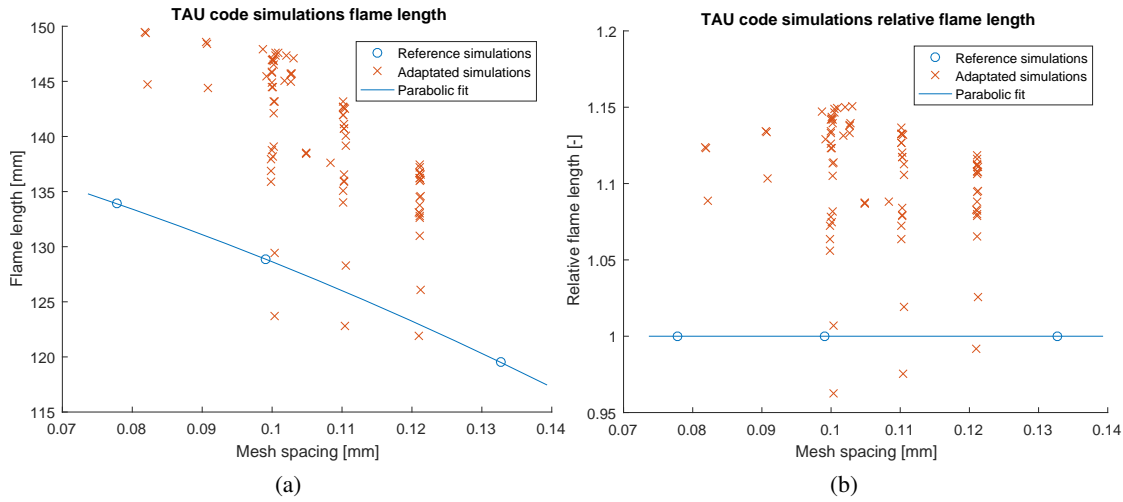


Figure 3.17: Flame length for TAU code simulations compared to the reference curve: (a) absolute values, (b) relative values.

reference curve fit. Figure 3.17a shows the flame length for all simulations, compared to the reference flame length curve. The relative flame length,  $F_{rel}$ , was calculated for every simulation dividing the calculated flame length by the reference one. It was used as criteria to determine the best value for each parameter, the larger the relative flame length, the better the solution Figure 3.17b shows the relative flame length for all the simulations.

The best values for the adaptation parameter "indicator user-values" are temperature and combinations of temperature with the species mass fractions. Only the temperature and the species mass fractions were tested for this parameters, since it was already known from the ANSYS CFX simulations that these parameters are the most influential ones to the mesh adaptation. More focus was given on understanding the TAU code specific adaptation parameters, so only few combinations "indicator user-values" of parameters were tested. The relative flame length calculated for the "indicator user-values" simulations is presented in the Figure 3.18.

For the parameter "indicator type", four sets of simulations were performed and are presented in the Table 3.11. The calculated relative flame for the solutions using the "indicator value" parameter as "diff" and "recon" were very similar, showing that there is no much difference on the solution whether the adaptation criteria is the differences of variables at the nodes or the reconstruction of the variable at the edge midface. Figure 3.19 presents the relative flame length for the "indicator type" simulations. The value "recon" is the best value for the "indicator type" parameter.

Three sets of simulations were made for testing the influence of the parameter "h-scaling power", they are presented in the Table 3.12. The only difference between the sets is the number of adaptations steps made, and it was observed that for sets 1 and 2, the best value for "h-scaling power" is 1, while for set 3 the best value is 0.5. The larger relative flame length was obtained for "h-scaling power" equals 0.5 and three adaptation steps, and the value of 0.5 was then considered the best value for this parameter. Also, 0.5 is the TAU code standard value for "h-scaling power". The comparison of relative flames for the "h-scaling power" simulations is presented in

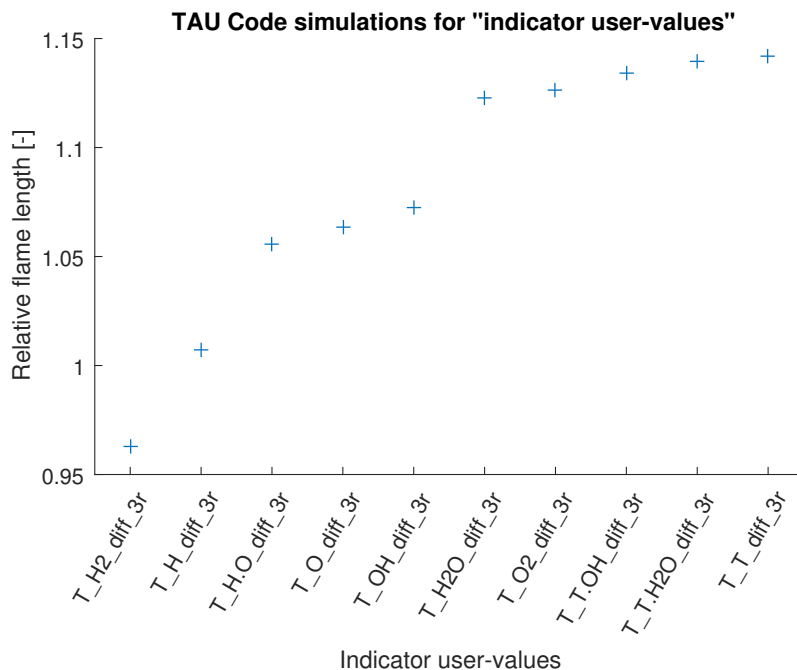
Figure 3.18: Comparison of  $F_{rel}$  for different values of "indicator user-values".

Table 3.11: Parameters of the simulations for "indicator type" tests.

Set	Simulation	Indicator user-values	Indicator type	Percent. of new points	h-scaling power	$F_{rel}$
1	T_T_diff_3s	temperature	diff	3×25	0.5	1.1419
	T_T_grad_3s	temperature	grad	3×25	0.5	1.1137
	T_T_recon_3s	temperature	recon	3×25	0.5	1.1425
2	T_OH_diff_3s	OH mass frac.	diff	3×25	0.5	1.0722
	T_OH_grad_3s	OH mass frac.	grad	3×25	0.5	1.0744
	T_OH_recon_3s	OH mass frac.	recon	3×25	0.5	1.0782
3	T_T.H2O_diff_3s	temperature, H <sub>2</sub> O mass fraction	diff	3×25	0.5	1.1397
	T_T.H2O_grad_3s	temperature, H <sub>2</sub> O mass fraction	grad	3×25	0.5	1.1052
	T_T.H2O_recon_3s	temperature, H <sub>2</sub> O mass fraction	recon	3×25	0.5	1.1425
4	T_H2O_diff_3s	H <sub>2</sub> O mass frac.	diff	3×25	0.5	1.1230
	T_H2O_grad_3s	H <sub>2</sub> O mass frac.	grad	3×25	0.5	1.0815
	T_H2O_recon_3s	H <sub>2</sub> O mass frac.	recon	3×25	0.5	1.1232

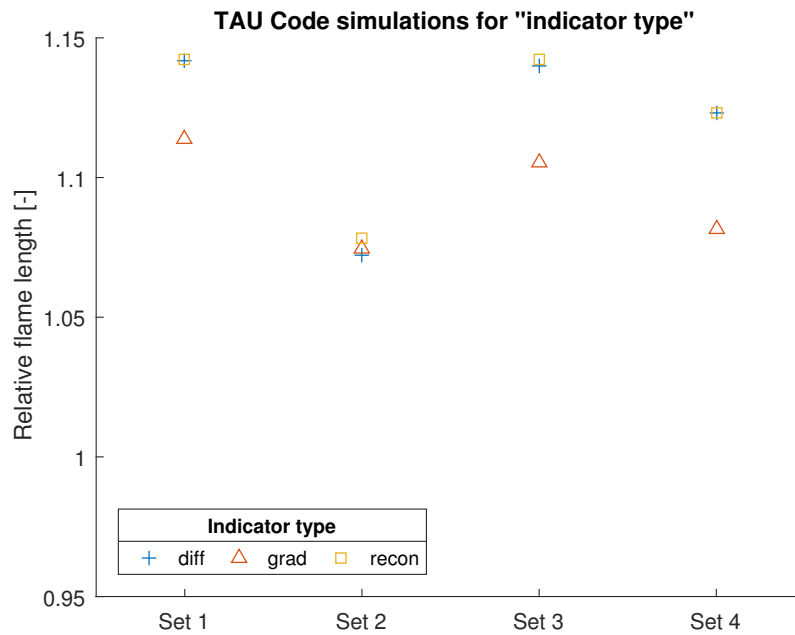


Figure 3.19: Comparison of  $F_{rel}$  for different values of "indicator type".

the Figure 3.20.

The ideal number of steps was tested together with the parameter "percentage of new points". As presented in the Table 3.13, for the sets 1, 2 and 3 the "percentage of new points" was fixed to 25 and the number of adaptation varied from 1 to 5. In general, the flame length increases when more nodes are added, but the larger relative flame lengths were obtained for the simulations with three adaptation steps. After these tests, the mesh resulting from the adaptation simulation T\_T\_diff\_3s was used for adaptation steps with the parameter "percentage of new points" set to 0. When this parameter is set to 0, the TAU code is only allowed to move nodes, removing them from some edges and adding them in others. Results using this strategy vary, with small changes in the flame length, but in general the results are not worth the increase in computational time. A third strategy tested was to add more node in the first steps, than less node in later steps. For this tests, simulations adding 75% of new nodes in the first adaptation followed by two steps adding 5% of nodes were performed. The obtained results showed this later method to be the best of the three methods tested. The relative flame length for all "percentage of new nodes" tested values is presented in the Figure 3.21. For all the tests, the value for the "indicator user-value" parameter is "temperature".

The parameter "refinement mode" was only tested with the value "both", allowing the TAU code to both add and remove node as needed. Other values for this parameter were not tested, since they would narrow the TAU code capability and the idea of this work is to give the adaptation code more flexibility to change the mesh. A summary of the best values for the parameters is presented in the Table 3.14.

Some parameters have more influence on the final relative flame length than others. For example, the solution for the "indicator type" simulations using values of "diff" and "recon" have

Table 3.12: Parameters of the simulations for "h-scaling power" tests.

Set	Simulation	Indicator user-values	Indicator type	Percent. of new points	h-scaling power	$F_{rel}$
1	T_T_diff_1s	temperature	diff	1×25	0.5	1.1124
	T_T_a1_1s	temperature	diff	1×25	1	1.1162
	T_T_a0_1s	temperature	diff	1×25	0	1.1081
2	T_T_diff_2s	temperature	diff	2×25	0.5	1.1324
	T_T_a1_2s	temperature	diff	2×25	1	1.1367
	T_T_a0_2s	temperature	diff	2×25	0	1.1270
3	T_T_diff_3s	temperature	diff	3×25	0.5	1.1419
	T_T_a1_3s	temperature	diff	3×25	1	1.1135
	T_T_a0_3s	temperature	diff	3×25	0	1.1333

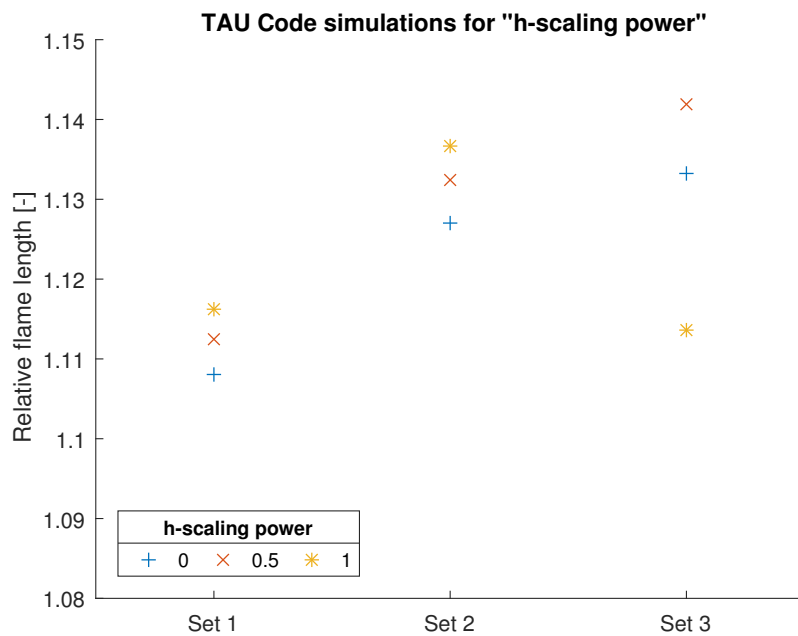
Figure 3.20: Comparison of  $F_{rel}$  for different values of "h-scaling power".

Table 3.13: Parameters of the simulations for "percentage of new points" tests.

Set	Simulation	Indicator type	Percent. of new points	h-scaling power	Num. of Nodes	$F$ [mm]	$F_{rel}$
1	T_T_diff_1s	diff	$1 \times 25$	0.5	91 k	136.74	1.1124
	T_T_diff_2s	diff	$2 \times 25$	0.5	106 k	142.62	1.1324
	T_T_diff_3s	diff	$3 \times 25$	0.5	124 k	146.82	1.1419
	T_T_diff_3s	diff	$4 \times 25$	0.5	146 k	148.41	1.1334
	T_T_diff_3s	diff	$5 \times 25$	0.5	175 k	149.38	1.1232
2	T_T_grad_1s	grad	$1 \times 25$	0.5	91 k	134.57	1.0950
	T_T_grad_2s	grad	$2 \times 25$	0.5	106 k	140.10	1.1129
	T_T_grad_3s	grad	$3 \times 25$	0.5	124 k	143.16	1.1137
	T_T_grad_4s	grad	$4 \times 25$	0.5	146 k	144.39	1.1031
	T_T_grad_5s	grad	$5 \times 25$	0.5	174 k	144.72	1.0887
3	T_T_recon_1s	recon	$1 \times 25$	0.5	91 k	136.70	1.1120
	T_T_recon_2s	recon	$2 \times 25$	0.5	106 k	142.66	1.1326
	T_T_recon_3s	recon	$3 \times 25$	0.5	124 k	146.94	1.1425
	T_T_recon_4s	recon	$4 \times 25$	0.5	146 k	148.53	1.1342
	T_T_recon_5s	recon	$5 \times 25$	0.5	175 k	149.49	1.1240
4	T_T_diff_3s_1s0	diff	$3 \times 25 + 1 \times 0$	0.5	124 k	147.05	1.1434
	T_T_diff_3s_2s0	diff	$3 \times 25 + 2 \times 0$	0.5	124 k	146.91	1.1419
5	T_T_75_1s	diff	$1 \times 75$	0.5	114 k	138.43	1.0868
	T_T_75.5_2s	diff	$1 \times 75 + 1 \times 5$	0.5	119 k	145.59	1.1380
	T_T_75.5.5_3s	diff	$1 \times 75 + 2 \times 5$	0.5	123 k	147.35	1.1464

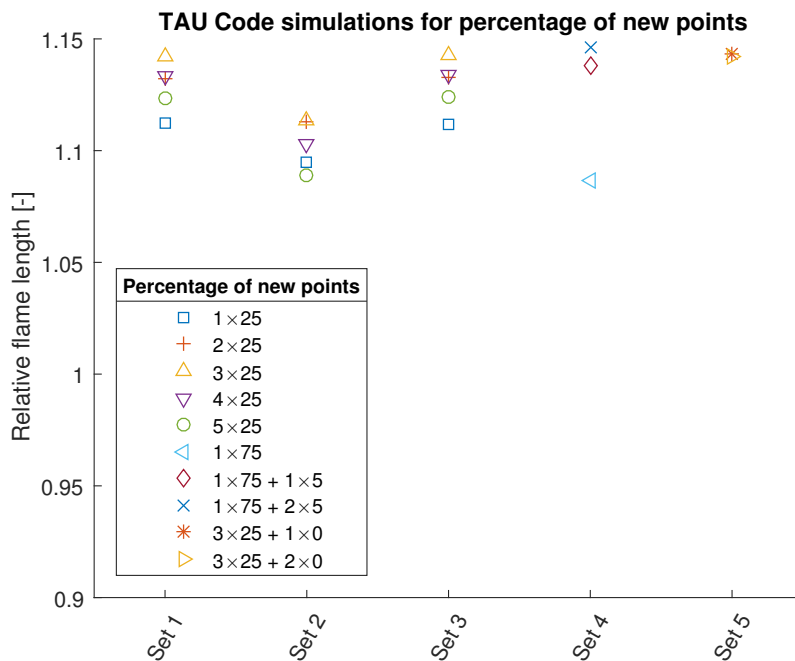
Figure 3.21: Comparison of  $F_{rel}$  for different values of "percentage of new points".

Table 3.14: Best values for TAU code adaptation parameters.

Parameter	Tested values
Indicator user-values	Temperature Temperature and H <sub>2</sub> mass fraction Temperature and OH Mass Fraction
Indicator type	recon
h-scaling power	0.5
Percentage of new points	$1 \times 75 + 2 \times 5$
Refinement mode	both

relative flame lengths with a difference smaller than 0.5%. For other parameter, as the parameter "indicator user-values", the difference between the smallest and the largest relative flame length is near to 20%. The parameter "h-scaling factor" was the only parameter for which there was no universal best value. From the three sets of simulations, two different best values of "h-scaling factor" could be identified, depending on the number of steps for the simulation. Even if, in average, 0.5 was the best value, both values were used for further simulations.

### 3.2.2.1 TAU code dynamical adaptation

The dynamical adaptation was also tested for the TAU code adaptation process. Two sets of simulations were performed for testing this strategy and they are presented in the Table 3.15. For the dynamical adaptation simulations, all new nodes were added during the first 10 adaptation steps, all later steps added no more nodes, they were only allowed to move them. Each simulation step was set to run only 100 iterations, then the mesh would be adapted based on the current solution. This number of iterations is not enough to converge the solution in a single step round, but the convergence was observed after several loops of adaptations. This method showed to be efficient when applied with the TAU code, demanding less computational time than the other methods and leading to the conjunct convergence of the mesh and the solution.

Table 3.15: Parameters for the TAU code dynamical simulations

Set	Simulation	Indicator user-values	Indicator type	Percent. of new points	h-scaling power	$F_{rel}$
1	T_T_diff_100i_200s	temperature	diff	$10 \times 7 + 190 \times 0$	0.5	1.1329
	T_T_diff_100i_300s	temperature	diff	$10 \times 7 + 290 \times 0$	0.5	1.1506
2	T_T_recon_100i_200s	temperature	recon	$10 \times 7 + 190 \times 0$	0.5	1.1315
	T_T_recon_100i_300s	temperature	recon	$10 \times 7 + 290 \times 0$	0.5	1.1501

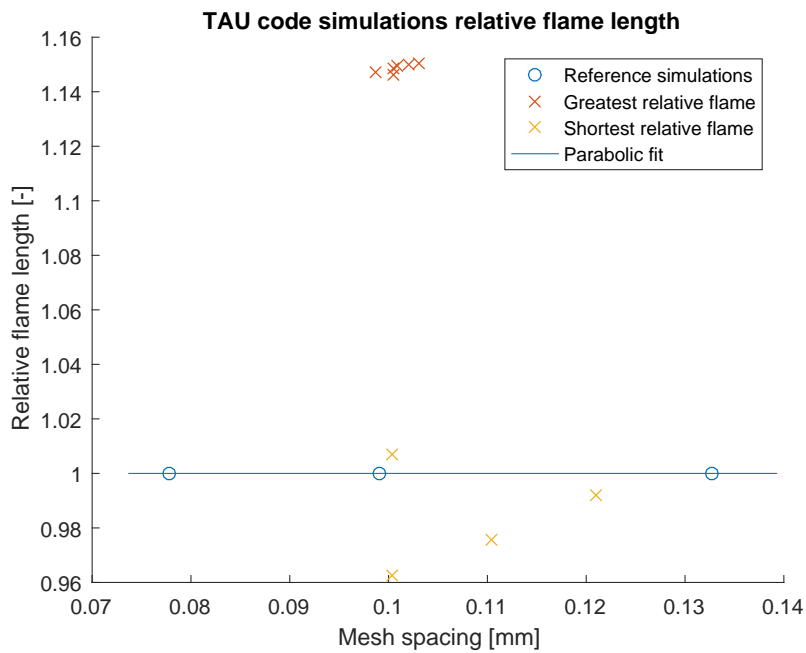


Figure 3.22: TAU code simulations with the largest and smallest reference flame length.

### 3.2.3 TAU code simulation results

A simulation was made using the best values for TAU code adaptation parameters, named `T_T_recon_75.5.5_3s`. Additional simulations were performed, using 0.5 and 1 as values for the parameter "h-scaling". The calculated flame length for all the simulations was compared to the reference curve fit. The simulations with largest and smallest relative flame length are presented in the Figure 3.22. More details of the results of these simulations are presented in the Table 3.16.

The largest value for  $F_{rel}$  was obtained for the simulation `T_T_diff_100i_300s`. This simulation was performed using the dynamical adaptation strategy, so results for a normal simulation, the `T_T_recon_a1_75.5.5_3s`, are also presented. The smallest relative flame length was obtained for the simulation `T_H2_diff_3s`. The temperature distribution and meshes for these three cases are presented in the Figure 3.23. For the simulations `T_T_diff_100i_300s` and `T_T_recon_a1_75.5.5_3s` it is possible to notice the mesh refinement surrounding the region where the temperature reaches 2000 K. For the simulation `T_H2_diff_3s`, the mesh is more refined near the wall, due to the change in  $H_2$  concentration, as can be seen in the Figure 3.16.

The temperature development along the symmetry axis for the simulations `T_T_diff_100i_300s`, `T_T_recon_a1_75.5.5_3s` and `T_H2_diff_3s` was compared to those from the TAU code reference meshes. These temperatures along a line between 80 mm and 170 mm are presented in the Figure 3.24. The temperature curves for the simulations `T_T_diff_100i_300s` and `T_T_recon_a1_75.5.5_3s` are very similar, being practically identical above  $T = 1500$  K. All the temperature curves presented follow a similar development, with a region of gradual increase in the variation of the temperature, a linear region and a region where the variation of the temperature decreases. These three regions can be divided by  $T \approx 1500$  K and  $T \approx 2500$  K. The main



Table 3.16: TAU code reference meshes and adaptation simulations with the largest and smallest relative flame lengths.

Simulation	Number of nodes	Number of elements	$F_{rel}$	$F$ [mm]	$F_{i,T}$ [%]	$h$ [mm]
TO1	80 k	115 k	1.000	119.51	-	0.133
TO2	132 k	207 k	1.000	128.89	7.85	0.099
TO3	199 k	335 k	1.000	133.91	12.05	0.078
T_T_diff_100i_300s	118 k	191 k	1.151	147.12	23.11	0.103
T_T_recon_100i_300s	120 k	194 k	1.150	147.34	23.29	0.102
T_T_recon_a1_75.5.5_3s	123 k	199 k	1.149	147.59	23.50	0.101
T_T_recon_75.5.5_3s	123 k	200 k	1.149	147.61	23.51	0.101
T_T_recon_a1_100i_300s	127 k	208 k	1.147	147.95	23.80	0.099
T_T_diff_75.5.5_3s	123 k	201 k	1.146	147.35	23.30	0.100
		...				
T_H_diff_3s	124 k	201 k	1.000	119.51	8.33	0.100
T_H2_diff_1s	92 k	138 k	0.992	121.94	2.04	0.121
T_H2_diff_2s	106 k	166 k	0.975	122.82	2.78	0.110
T_H2_diff_3s	124 k	201 k	0.963	123.75	3.55	0.100

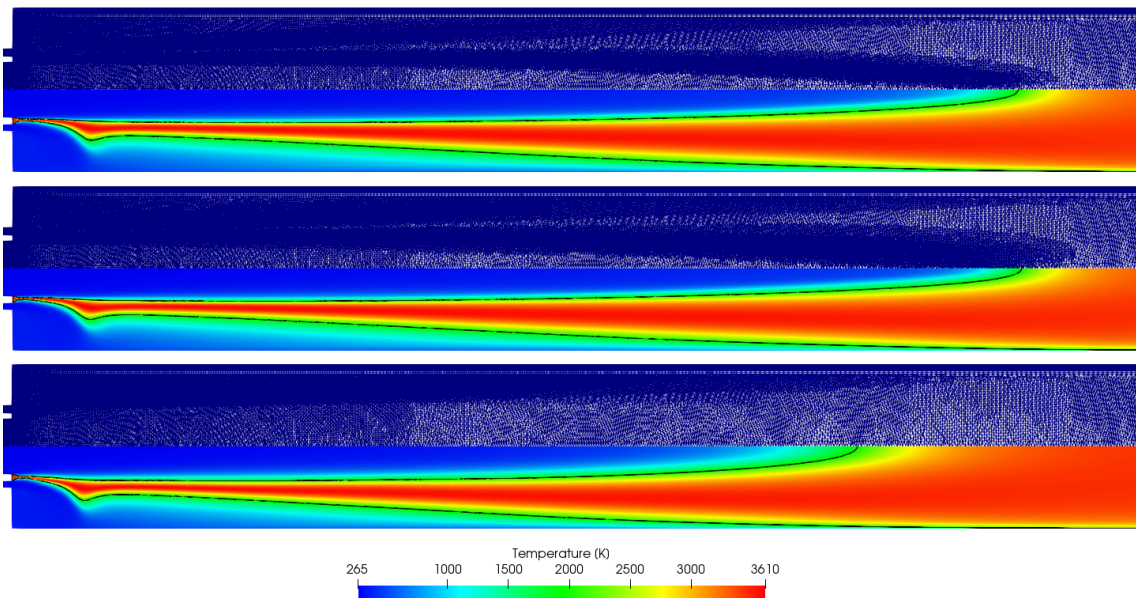


Figure 3.23: Temperature distribution, a line of  $T = 2000$  K and the mesh of the simulations T\_T\_diff\_100i\_300s (top), T\_T\_recon\_a1\_75.5.5\_3s (middle) and T\_H2\_diff\_3s (bottom). The axial direction is clinched by a factor of 2.

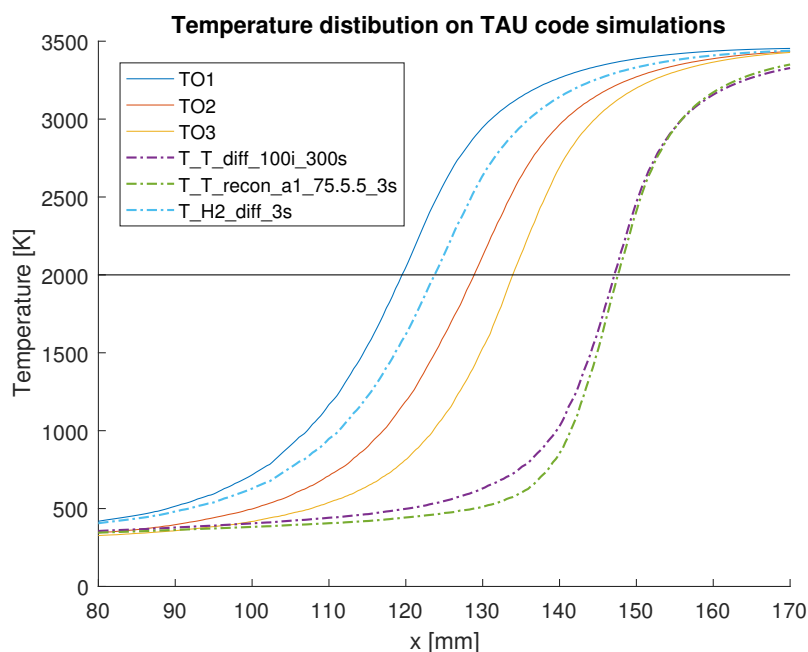


Figure 3.24: Temperature distribution along a central line for the best, worst and reference TAU code simulations.

difference in these temperature curves is the offset of the linear regions and their inclinations, that are steeper for the simulations with longer flames.

### 3.2.4 TAU code simulations conclusions

The TAU code was capable of adapting the mesh for combustion simulations. Some parameters have more influence on the final solution than others, but the final mesh obtained is greatly dependant on the selected values for the adaptation parameters. The parameter "indicator user-values" is the one with more influence on the final solution.

After test simulations, the best values for the adaptation parameters were determined and are presented in the Table 3.14. The relative flame length was calculated for each simulation, using the simulation flame length and the reference flame length, calculated from the reference meshes. The largest value obtained for the relative flame length was 1.151 and the worst value was 0.963. The strategy of dynamical adaptations was also tested, and the results showed to be successful, resulting a conjoint convergence of the mesh and the solution, in fewer iterations than the reference adaptation strategy.

Adapting the mesh of the studied case using the TAU code increased the flame length for up to 15% when compared to the expected flame length of a mesh refined with no adaptation. The TAU code mesh adaptation showed to be a positive strategy, adding nodes in regions of the mesh where they impact more the final solution.

## Chapter 4

# Conclusions

This work presented the use of mesh adaptation algorithms for rocket combustion chambers simulations. The simulations were performed using the commercial code ANSYS CFX and the in-house code of DLR, the TAU code. The ANSYS CFX simulations were performed using the same study case of Zhukov and Heinrich [23], while the TAU code study case was based on an experimental rocket combustion chamber studied at TU München [20].

Meshes with different levels of refinement were used to determine reference solutions, and the flame lengths of all the adaptation simulation were calculated. A relative flame length was defined, to compare the flame length obtained from an adapted mesh to that expected from a regular refined mesh with similar mean mesh spacing.

Simulations have been performed for both studied cases, to define the best values for the adaptation parameters. These values are presented in the Table 4.1 for ANSYS CFX and in Table 4.2 for TAU code simulations. Other strategies as smoothing the adapted mesh and dynamical adaptation were also tested.

Both software were capable of adapting the studied meshes for combustion simulations. It was observed that some parameter have more influence on the final mesh than others and that the selection of values for the adaptation parameter have a great impact on the obtained mesh. So the choice of the values of the parameters is an important step of the adaptation process.

The largest flame lengths obtained after the ANSYS CFX adaptation showed values similar to those of the reference simulations. That is, for the studied case, the ANSYS CFX mesh adaptation process is not efficient, consuming more computer time than a simulation in a regularly refined mesh of same mesh spacing. Smoothing the adapted mesh showed to improve the final results, but this task is time demanding from the user, and that is considered to be out of the scope of this work. No convergence was obtained when the dynamical adaptation was tested with ANSYS CFX.

The TAU code adaptation simulations showed longer flames than those of reference. An increase of up to 15% in flame length, compared to the expected value for a mesh with similar mesh spacing, was achieved. The dynamical adaptation using the TAU code showed to be a good strategy, achieving some of the best results for the studied case, with less iterations needed. Further studies on the use of the TAU code mesh adaptation for combustion chamber are recommended.

Table 4.1: Best values for ANSYS CFX adaptation parameters.

Parameter	Best value
Variable list	Temperature, H <sub>2</sub> O Molar Fraction and H <sub>2</sub> Molar Fraction H <sub>2</sub> O Molar Fraction and H <sub>2</sub> Molar Fraction Temperature, H <sub>2</sub> O Molar Fraction and O <sub>2</sub> Molar Fraction Temperature, H <sub>2</sub> Molar Fraction and O <sub>2</sub> Molar Fraction Temperature and H <sub>2</sub> O Molar Fraction H <sub>2</sub> O Molar Fraction Temperature H <sub>2</sub> O Molar Fraction and O <sub>2</sub> Molar Fraction Temperature, O <sub>2</sub> Molar Fraction
Maximum number of step	5
Adaptation method	Solution variable $\times$ Length
Node allocation parameter	2
Number of levels	1

Table 4.2: Best values for TAU code adaptation parameters.

Parameter	Tested values
Indicator user-values	Temperature Temperature and H <sub>2</sub> mass fraction Temperature and OH Mass Fraction
Indicator type	recon
h-scaling power	0.5
Percentage of new points	$1 \times 75 + 2 \times 5$
Refinement mode	both

## **Appendix A**

# **List of ANSYS CFX adaptation simulations**

The ANSYS CFX simulations are name based on the variables select for the adaptation criteria and the number of simulations already performed with these same variables. The letter A at the beginning of the names identifies the ANSYS CFX simulations. For example, A\_T.H2O\_03 is the third simulation using temperature (T) and H<sub>2</sub>O molar fraction (H2O) as adaptation variables. Special cases are also noted on the names of the simulations. The dynamical adaptations are marked by a "dyn" and the smoothed meshes by an "S" in their names.

An explanation on the used parameter is available in the section 2.4.3.1.

Simulation	Variable List	Max. Num. Step	Adap. method	Max. Iter.	Node Factor	Num. of levels	Num. of nodes	Num. of elements	$F$ [mm]	$F_{i,A}$ [%]	$h$ [mm]	$F_{rel}$ [mm]
AO1	-	-	-	-	-	-	301 k	1.45 M	30.15	0.00	0.125	0.998
AO2	-	-	-	-	-	-	385 k	2.046 M	33.98	12.72	0.111	1.004
AO3	-	-	-	-	-	-	651 k	3.51 M	38.27	26.94	0.093	0.996
AO4	-	-	-	-	-	-	1.128 M	6.161 M	42.10	39.64	0.077	1.001
A_D_01	Density	5	Var×Len	1000	1	1	901 k	4.063 M	34.71	15.13	0.089	0.880
A_dyn_T.H2O_01 <sup>1</sup>	Temperature, H <sub>2</sub> O molar fraction	10000	Var×Len	20	2	1	-	-	-	-	-	-
A_dyn_T.H2O_02 <sup>1</sup>	Temperature, H <sub>2</sub> O molar fraction	10000	Var×Len	50	2	1	-	-	-	-	-	-
A_dyn_T.H2O_03 <sup>1</sup>	Temperature, H <sub>2</sub> O molar fraction	1000	Var×Len	1	2	1	-	-	-	-	-	-
A_dyn_T.H2O_04 <sup>1</sup>	Temperature, H <sub>2</sub> O molar fraction	1000	Var×Len	1	2	2	-	-	-	-	-	-
A_dyn_T.H2O_05 <sup>1</sup>	Temperature, H <sub>2</sub> O molar fraction	1000	Var	1	2	1	-	-	-	-	-	-
A_dyn_T.H2O_06 <sup>1</sup>	Temperature, H <sub>2</sub> O molar fraction	1000	Var	1	2	2	-	-	-	-	-	-
A_dyn_T.H2O_07 <sup>1</sup>	Temperature, H <sub>2</sub> O molar fraction	1000	Var	100	2	1	-	-	-	-	-	-
A_dyn_T_01	Temperature	10	Var×Len	100	10	1	882 k	4.432 M	38.57	27.95	0.086	0.963
A_dyn_T_02 <sup>1</sup>	Temperature	10000	Var×Len	10	10	1	-	-	-	-	-	-

Simulation	Variable List	Max. Num. Step	Adap. method	Max. Iter.	Node Factor	Num. of levels	Num. of nodes	Num. of elements	$F$ [mm]	$F_{i,A}$ [%]	$h$ [mm]	$F_{rel}$ [mm]
A_dyn_T_03 <sup>1</sup>	Temperature	10000	Var×Len	20	20	1	-	-	-	-	-	-
A_EV_01	Eddy Viscosity	5	Var×Len	1000	1	1	880 k	4.46 M	31.77	5.38	0.086	0.793
A_H2.O2_01	H <sub>2</sub> molar fraction, O <sub>2</sub> molar fraction	5	Var×Len	1000	1	1	648 k	3.228 M	36.67	21.64	0.096	0.971
A_H2_01	H <sub>2</sub> molar fraction	5	Var×Len	1000	1	1	898 k	4.564 M	33.73	11.90	0.085	0.839
A_H2O.H2_01	H <sub>2</sub> O molar fraction, O <sub>2</sub> molar fraction	5	Var×Len	1000	1	1	892 k	4.473 M	40.09	32.99	0.086	1.000
A_H2O.O2_01	H <sub>2</sub> O molar fraction, H <sub>2</sub> molar fraction	5	Var×Len	1000	1	1	893 k	4.477 M	39.82	32.07	0.086	0.993
A_H2O_01	H <sub>2</sub> O molar fraction	5	Var×Len	1000	1	1	890 k	4.477 M	39.96	32.55	0.086	0.996
A_HORR_01	Hydrogen Oxigen, Reaction Rate	5	Var×Len	1000	1	1	892 k	4.493 M	33.06	9.67	0.086	0.824
A_O2_01	O <sub>2</sub> molar fraction	5	Var×Len	1000	1	1	887 k	4.504 M	36.59	21.36	0.086	0.911
A_S_T.H2O_03_01 <sup>2</sup>	-	-	-	-	-	-	845 k	4.362 M	40.24	33.46	0.086	1.008
A_S_T.H2O_03_02 <sup>3</sup>	Temperature, H <sub>2</sub> O molar fraction	5	Var×Len	1000	1	1	1.644 M	8.476 M	41.91	39.00	0.069	0.958
A_SEntr_01	Static Entropy	5	Var×Len	1000	1	1	889 k	4.47 M	35.62	18.16	0.086	0.889
A_T.H2.O2_01	Temperature, H <sub>2</sub> molar fraction, O <sub>2</sub> molar fraction	5	Var×Len	1000	1	1	895 k	4.501 M	40.02	32.75	0.086	0.997

Simulation	Variable List	Max. Num. Step	Adap. method	Max. Iter.	Node Factor	Num. of levels	Num. of nodes	Num. of elements	$F$ [mm]	$F_{i,A}$ [%]	$h$ [mm]	$F_{rel}$ [mm]
A_T.H2_01	Temperature, H <sub>2</sub> molar fraction	5	Var×Len	1000	1	1	894 k	4.496 M	39.58	31.28	0.086	0.986
A_T.H2O.H2_01	Temperature, H <sub>2</sub> O molar fraction, H <sub>2</sub> molar fraction	5	Var×Len	1000	1	1	892 k	4.475 M	40.21	33.37	0.086	1.003
A_T.H2O.H2_02	Temperature, H <sub>2</sub> O molar fraction, H <sub>2</sub> molar fraction	5	Var×Len	1000	2	1	900 k	4.519 M	40.35	33.83	0.085	1.005
A_T.H2O.O2_01	Temperature, H <sub>2</sub> O molar fraction, O <sub>2</sub> molar fraction	5	Var×Len	1000	1	1	893 k	4.474 M	40.00	32.69	0.086	0.998
A_T.H2O_01	Temperature, H <sub>2</sub> O molar fraction	5	Var×Len	1000	1	2	588 k	2.935 M	33.93	12.54	0.099	0.916
A_T.H2O_02	Temperature, H <sub>2</sub> O molar fraction	5	Var×Len	1000	1	2	865 k	4.361 M	37.41	24.07	0.087	0.937
A_T.H2O_03	Temperature, H <sub>2</sub> O molar fraction	5	Var×Len	1000	1	1	891 k	4.477 M	39.97	32.57	0.086	0.997
A_T.H2O_04 <sup>4</sup>	Temperature, H <sub>2</sub> O molar fraction	5	Var×Len	1000	1	1	1.736 M	8.814 M	41.72	38.37	0.068	0.950
A_T.H2O_05	Temperature, H <sub>2</sub> O molar fraction	10	Var×Len	1000	1	1	899 k	4.536 M	40.12	33.07	0.085	0.998



Simulation	Variable List	Max. Num. Step	Adap. method	Max. Iter.	Node Factor	Num. of levels	Num. of nodes	Num. of elements	$F$ [mm]	$F_{i,A}$ [%]	$h$ [mm]	$F_{rel}$ [mm]
A_T.H2O_06	Temperature, H <sub>2</sub> O molar fraction	5	Var	1000	1	1	883 k	4.409 M	39.58	31.29	0.086	0.989
A_T.H2O_07	Temperature, H <sub>2</sub> O molar fraction	5	Var	1000	1	2	879 k	4.45 M	34.35	13.94	0.086	0.857
A_T.H2O_08	Temperature, H <sub>2</sub> O molar fraction	5	Var×Len	1000	1	2	870 k	4.386 M	37.32	23.80	0.086	0.934
A_T.H2O_09	Temperature, H <sub>2</sub> O molar fraction	5	Var×Len	1000	2	1	902 k	4.537 M	40.08	32.95	0.085	0.997
A_T.H2O_10	Temperature, H <sub>2</sub> O molar fraction	5	Var	1000	2	1	893 k	4.46 M	39.76	31.87	0.086	0.992
A_T.H2O_11	Temperature, H <sub>2</sub> O molar fraction	5	Var×Len	1000	1	1	1.202 M	6.104 M	40.57	34.56	0.077	0.966
A_T.H2O_12	Temperature, H <sub>2</sub> O molar fraction	5	Var×Len	1000	1	2	1.152 M	5.819 M	36.72	21.81	0.079	0.880
A_T.H2O_13	Temperature, H <sub>2</sub> O molar fraction	5	Var×Len	1000	3	1	916 k	4.615 M	40.19	33.32	0.085	0.997
A_T.H2O_14	Temperature, H <sub>2</sub> O molar fraction	5	Var	1000	3	1	900 k	4.499 M	39.92	32.68	0.086	0.995
A_T.O2_01	Temperature, O <sub>2</sub> molar fraction	5	Var×Len	1000	1	2	588 k	2.931 M	34.43	14.22	0.099	0.930
A_T.O2_02	Temperature, O <sub>2</sub> molar fraction	5	Var×Len	1000	1	1	901 k	4.537 M	39.87	32.25	0.085	0.992

Simulation	Variable List	Max. Num. Step	Adap. method	Max. Iter.	Node Factor	Num. of levels	Num. of nodes	Num. of elements	$F$ [mm]	$F_{i,A}$ [%]	$h$ [mm]	$F_{rel}$ [mm]
A_T.V_01	Temperature, Velocity	5	Var×Len	1000	1	1	890 k	4.485 M	39.57	31.26	0.086	0.987
A_T.Vo_01	Temperature, Vorticity	5	Var×Len	1000	1	1	887 k	4.435 M	39.61	31.40	0.086	0.989
A_T_01	Temperature	4	Var×Len	200	0	3	588 k	2.941 M	33.70	11.80	0.099	0.910
A_T_02	Temperature	5	Var×Len	1000	1	1	894 k	4.506 M	39.89	32.30	0.086	0.994
A_TEnth_01	Total Enthalpy	5	Var×Len	1000	1	1	905 k	4.551 M	39.41	30.72	0.085	0.980
A_V_01	Velocity	5	Var×Len	1000	1	1	896 k	4.551 M	36.80	22.08	0.085	0.915
A_Vo_01	Vorticity	5	Var×Len	1000	1	1	934 k	4.554 M	35.76	18.61	0.085	0.889
A_Vvw_01	$\sqrt{v^2 + w^2}$	5	Var×Len	1000	1	1	892 k	4.484 M	33.11	9.81	0.086	0.825

<sup>1</sup>No convergence obtained.

<sup>2</sup>Resulting mesh from A\_T.H<sub>2</sub>O\_03, smoothed in ICEM CFD. Simple run, no adaptation. Results from A\_T.H<sub>2</sub>O\_03 as initial values.

<sup>3</sup>Similar to A\_T.H<sub>2</sub>O\_03, using A\_S.T.H<sub>2</sub>O\_03\_01 mesh for adaptation. Results from A\_T.H<sub>2</sub>O\_03 as initial values.

<sup>4</sup>Similar to A\_T.H<sub>2</sub>O\_03, using A\_T.H<sub>2</sub>O\_03 mesh for adaptation. Results from A\_T.H<sub>2</sub>O\_03 as initial values.

## Appendix B

# List of TAU code adaptation simulations

The names of the TAU code simulations are based on the values for the changed adaptation parameters in the simulation. The letter T at the beginning of the names identifies the TAU code simulations. For example, the simulation T\_T\_diff\_1s uses temperature (T) as adaptation variable, "diff" as indicator type and one adaptation step (1s). The simulation T\_T\_recon\_a1\_75.5.5\_3s uses temperature (T) as adaptation variable, "recon" as indicator type, considers the "h-scaling power" –  $\alpha$  in (2.30) – as 1 (a1) and was performed in three steps (3s) adding 75% of new nodes on the first step and 5% on the second and third steps. The dynamical simulations are named based also on the number of iterations per step, for example, T\_T\_diff\_100i\_200s is a dynamical simulation with 200 steps (200s) and each of them had 100 iterations (100i).

An explanation on the used parameter is available in the section 2.4.3.2.

Simulation	Indic. user-values	Perc. of new points	Refine. Mode	h-scaling power	Num. of levels	Num. of nodes	Num. of elements	$F$ [mm]	$F_{i,A}$ [%]	$h$ [mm]	$F_{rel}$ [mm]
TO1	-	-	-	-	-	80 k	115 k	119.51	0.00	0.133	1.000
TO <sub>2</sub>	-	-	-	-	-	132 k	207 k	128.89	7.85	0.099	1.000
TO3	-	-	-	-	-	199 k	335 k	133.91	12.05	0.078	1.000
T_T_diff_1s	Temperature	1×25	both	diff	0.5	91 k	138 k	136.74	14.42	0.121	1.112
T_T_diff_2s	Temperature	2×25	both	diff	0.5	106 k	167 k	142.62	19.34	0.110	1.132
T_T_diff_3s	Temperature	3×25	both	diff	0.5	124 k	202 k	146.82	22.86	0.100	1.142
T_T_diff_4s	Temperature	4×25	both	diff	0.5	146 k	246 k	148.41	24.19	0.091	1.133
T_T_diff_5s	Temperature	5×25	both	diff	0.5	175 k	302 k	149.38	24.99	0.082	1.123
T_T_grad_1s	Temperature	1×25	both	grad	0.5	91 k	138 k	134.57	12.61	0.121	1.095
T_T_grad_2s	Temperature	2×25	both	grad	0.5	106 k	166 k	140.10	17.23	0.110	1.113
T_T_grad_3s	Temperature	3×25	both	grad	0.5	124 k	201 k	143.17	19.80	0.100	1.114
T_T_grad_4s	Temperature	4×25	both	grad	0.5	146 k	245 k	144.39	20.82	0.091	1.103
T_T_grad_5s	Temperature	5×25	both	grad	0.5	174 k	300 k	144.72	21.10	0.082	1.089
T_T_recon_1s	Temperature	1×25	both	recon	0.5	92 k	138 k	136.70	14.39	0.121	1.112
T_T_recon_2s	Temperature	2×25	both	recon	0.5	106 k	167 k	142.66	19.37	0.110	1.133
T_T_recon_3s	Temperature	3×25	both	recon	0.5	124 k	202 k	146.94	22.96	0.100	1.142
T_T_recon_4s	Temperature	4×25	both	recon	0.5	147 k	247 k	148.53	24.29	0.091	1.134
T_T_recon_5s	Temperature	5×25	both	recon	0.5	175 k	302 k	149.49	25.09	0.082	1.124
T_OH_diff_1s	OH mass fraction	1×25	both	diff	0.5	91 k	138 k	132.63	10.98	0.121	1.079

Simulation	Indic. user-values	Perc. of new points	Refine. Mode	h-scaling power	Num. of levels	Num. of nodes	Num. of elements	$F$ [mm]	$F_{i,A}$ [%]	$h$ [mm]	$F_{rel}$ [mm]
T_OH_diff_2s	OH mass fraction	2×25	both	diff	0.5	106 k	167 k	135.87	13.69	0.110	1.079
T_OH_diff_3s	OH mass fraction	3×25	both	diff	0.5	124 k	203 k	137.97	15.45	0.100	1.072
T_OH_grad_1s	OH mass fraction	1×25	both	grad	0.5	92 k	138 k	133.13	11.40	0.121	1.083
T_OH_grad_2s	OH mass fraction	2×25	both	grad	0.5	106 k	166 k	136.55	14.26	0.110	1.084
T_OH_grad_3s	OH mass fraction	3×25	both	grad	0.5	124 k	202 k	138.18	15.63	0.100	1.074
T_OH_recon_1s	OH mass fraction	1×25	both	recon	0.5	91 k	138 k	133.02	11.31	0.121	1.082
T_OH_recon_2s	OH mass fraction	2×25	both	recon	0.5	106 k	167 k	135.96	13.77	0.110	1.079
T_OH_recon_3s	OH mass fraction	3×25	both	recon	0.5	124 k	203 k	138.72	16.07	0.100	1.078
T_T.H2O_diff_1s	Temperature H <sub>2</sub> O mass fraction	1×25	both	diff	0.5	91 k	138 k	136.54	14.26	0.121	1.111
T_T.H2O_diff_2s	Temperature H <sub>2</sub> O mass fraction	2×25	both	diff	0.5	106 k	166 k	142.51	19.25	0.110	1.132
T_T.H2O_diff_3s	Temperature H <sub>2</sub> O mass fraction	3×25	both	diff	0.5	123 k	202 k	146.54	22.62	0.100	1.140
T_T.H2O_grad_1s	Temperature H <sub>2</sub> O mass fraction	1×25	both	grad	0.5	91 k	138 k	134.52	12.56	0.121	1.094
T_T.H2O_grad_2s	Temperature H <sub>2</sub> O mass fraction	2×25	both	grad	0.5	106 k	166 k	139.16	16.44	0.111	1.105
T_T.H2O_grad_3s	Temperature H <sub>2</sub> O mass fraction	3×25	both	grad	0.5	124 k	201 k	142.09	18.90	0.100	1.105

Simulation	Indic. user-values	Perc. of new points	Refine. Mode	h-scaling power	Num. of levels	Num. of nodes	Num. of elements	$F$ [mm]	$F_{i,A}$ [%]	$h$ [mm]	$F_{rel}$ [mm]
T_T.H2O_recon_1s	Temperature H <sub>2</sub> O mass fraction	1×25	both	recon	0.5	92 k	138 k	136.70	14.39	0.121	1.112
T_T.H2O_recon_2s	Temperature H <sub>2</sub> O mass fraction	2×25	both	recon	0.5	106 k	167 k	142.66	19.37	0.110	1.133
T_T.H2O_recon_3s	Temperature H <sub>2</sub> O mass fraction	3×25	both	recon	0.5	124 k	202 k	146.94	22.96	0.100	1.142
T_H2O_diff_1s	H <sub>2</sub> O mass fraction	1×25	both	diff	0.5	91 k	138 k	135.94	13.75	0.121	1.106
T_H2O_diff_2s	H <sub>2</sub> O mass fraction	2×25	both	diff	0.5	106 k	166 k	140.69	17.73	0.110	1.117
T_H2O_diff_3s	H <sub>2</sub> O mass fraction	3×25	both	diff	0.5	124 k	202 k	144.46	20.88	0.100	1.123
T_H2O_grad_1s	H <sub>2</sub> O mass fraction	1×25	both	grad	0.5	92 k	138 k	133.76	11.93	0.121	1.088
T_H2O_grad_2s	H <sub>2</sub> O mass fraction	2×25	both	grad	0.5	106 k	172 k	137.64	15.17	0.108	1.088
T_H2O_grad_3s	H <sub>2</sub> O mass fraction	3×25	both	grad	0.5	124 k	201 k	139.05	16.35	0.100	1.082
T_H2O_recon_1s	H <sub>2</sub> O mass fraction	1×25	both	recon	0.5	91 k	138 k	136.07	13.86	0.121	1.107
T_H2O_recon_2s	H <sub>2</sub> O mass fraction	2×25	both	recon	0.5	106 k	166 k	140.69	17.73	0.110	1.117
T_H2O_recon_3s	H <sub>2</sub> O mass fraction	3×25	both	recon	0.5	124 k	202 k	144.46	20.88	0.100	1.123
T_H_diff_1s	H mass fraction	1×25	both	diff	0.5	91 k	138 k	126.04	5.47	0.121	1.026
T_H_diff_2s	H mass fraction	2×25	both	diff	0.5	106 k	166 k	128.32	7.38	0.111	1.019
T_H_diff_3s	H mass fraction	3×25	both	diff	0.5	124 k	201 k	129.46	8.33	0.100	1.007
T_O_diff_1s	O mass fraction	1×25	both	diff	0.5	92 k	138 k	132.81	11.13	0.121	1.080

Simulation	Indic. user-values	Perc. of new points	Refine. Mode	h-scaling power	Num. of levels	Num. of nodes	Num. of elements	$F$ [mm]	$F_{i,A}$ [%]	$h$ [mm]	$F_{rel}$ [mm]
T_O_diff_2s	O mass fraction	2×25	both	diff	0.5	106 k	167 k	135.08	13.03	0.110	1.072
T_O_diff_3s	O mass fraction	3×25	both	diff	0.5	124 k	203 k	136.85	14.51	0.100	1.063
T_H.O_diff_1s	H mass fraction O mass fraction	1×25	both	diff	0.5	92 k	138 k	131.01	9.63	0.121	1.066
T_H.O_diff_2s	H mass fraction O mass fraction	2×25	both	diff	0.5	106 k	167 k	133.98	12.11	0.110	1.063
T_H.O_diff_3s	H mass fraction O mass fraction	3×25	both	diff	0.5	124 k	203 k	135.86	13.69	0.100	1.056
T_T.OH_diff_1s	Temperature OH mass fraction	1×25	both	diff	0.5	91 k	138 k	136.22	13.98	0.121	1.108
T_T.OH_diff_2s	Temperature OH mass fraction	2×25	both	diff	0.5	106 k	167 k	141.11	18.08	0.110	1.120
T_T.OH_diff_3s	Temperature OH mass fraction	3×25	both	diff	0.5	124 k	203 k	145.89	22.08	0.100	1.134
T_T_diff_3s_1s0	Temperature	3×25+1×0	both	diff	0.5	124 k	202 k	147.05	23.05	0.100	1.143
T_T_diff_3s_2s0	Temperature	3×25+2×0	both	diff	0.5	124 k	203 k	146.91	22.93	0.100	1.142
T_T_diff_75_1s	Temperature	1×75	both	diff	0.5	115 k	184 k	138.43	15.83	0.105	1.087
T_T_diff_75.5_2s	Temperature	1×75+1×5	both	diff	0.5	119 k	192 k	145.59	21.83	0.103	1.138
T_T_diff_75.5.5_3s	Temperature	1×75+2×5	both	diff	0.5	123 k	201 k	147.35	23.30	0.100	1.146
T_T_diff_100i_200s	Temperatue	10×7+190×0	both	diff	0.5	119 k	192 k	144.96	21.30	0.103	1.133

Simulation	Indic. user-values	Perc. of new points	Refine. Mode	h-scaling power	Num. of levels	Num. of nodes	Num. of elements	$F$ [mm]	$F_{i,A}$ [%]	$h$ [mm]	$F_{rel}$ [mm]
T_T_diff_100i_300s	Temperature	10×7+290×0	both	diff	0.5	118 k	191 k	147.12	23.11	0.103	1.151
T_T_diff_a1_1s	Temperature	1×25	both	diff	1	92 k	138 k	137.22	14.82	0.121	1.116
T_T_diff_a1_2s	Temperature	2×25	both	diff	1	106 k	167 k	143.19	19.82	0.110	1.137
T_T_diff_a1_3s	Temperature	3×25	both	diff	1	124 k	202 k	143.19	19.82	0.100	1.114
T_T_diff_a0_1s	Temperature	1×25	both	diff	0	92 k	138 k	136.23	13.99	0.121	1.108
T_T_diff_a0_2s	Temperature	2×25	both	diff	0	106 k	167 k	141.96	18.79	0.110	1.127
T_T_diff_a0_3s	Temperature	3×25	both	diff	0	124 k	203 k	145.79	22.00	0.100	1.133
T_O <sub>2</sub> _diff_1s	O <sub>2</sub> mass fraction	1×25	both	diff	0.5	91 k	138 k	137.49	15.05	0.121	1.118
T_O <sub>2</sub> _diff_2s	O <sub>2</sub> mass fraction	2×25	both	diff	0.5	106 k	167 k	141.92	18.75	0.110	1.127
T_O <sub>2</sub> _diff_3s	O <sub>2</sub> mass fraction	3×25	both	diff	0.5	124 k	203 k	144.91	21.26	0.100	1.126
T_H <sub>2</sub> _diff_1s	H <sub>2</sub> mass fraction	1×25	both	diff	0.5	92 k	138 k	121.94	2.04	0.121	0.992
T_H <sub>2</sub> _diff_2s	H <sub>2</sub> mass fraction	2×25	both	diff	0.5	106 k	166 k	122.82	2.78	0.110	0.975
T_H <sub>2</sub> _diff_3s	H <sub>2</sub> mass fraction	3×25	both	diff	0.5	124 k	201 k	123.75	3.55	0.100	0.963
T_T_recon_100i_200s	Temperature	10×7+190×0	both	recon	0.5	120 k	196 k	145.05	21.37	0.102	1.132
T_T_recon_100i_300s	Temperature	10×7+290×0	both	recon	0.5	120 k	194 k	147.34	23.29	0.102	1.150
T_T_recon_a1_100i_200s	Temperature	10×7+190×0	both	recon	1	126 k	206 k	145.49	21.75	0.099	1.129
T_T_recon_a1_100i_300s	Temperature	10×7+290×0	both	recon	1	127 k	208 k	147.95	23.80	0.099	1.147
T_T_recon_75_1s	Temperature	1×75	both	recon	0.5	115 k	184 k	138.47	15.87	0.105	1.087
T_T_recon_75.5_2s	Temperature	1×75+1×5	both	recon	0.5	119 k	192 k	145.67	21.89	0.103	1.139



<b>Simulation</b>	<b>Indic. user-values</b>	<b>Perc. of new points</b>	<b>Refine. Mode</b>	<b>h-scaling power</b>	<b>Num. of levels</b>	<b>Num. of nodes</b>	<b>Num. of elements</b>	$F$ [mm]	$F_{i,A}$ [%]	$h$ [mm]	$F_{rel}$ [mm]
T_T_recon_75.5.5_3s	Temperature	$1 \times 75 + 2 \times 5$	both	recon	0.5	123 k	200 k	147.61	23.51	0.101	1.149
T_T_recon_a1_75_1s	Temperature	$1 \times 75$	both	recon	1	115 k	184 k	138.52	15.91	0.105	1.087
T_T_recon_a1_75.5_2s	Temperature	$1 \times 75 + 1 \times 5$	both	recon	1	119 k	191 k	145.72	21.94	0.103	1.139
T_T_recon_a1_75.5.5_3s	Temperature	$1 \times 75 + 2 \times 5$	both	recon	1	123 k	199 k	147.59	23.50	0.101	1.149



# Bibliography

- [1] Procedure for Estimation and Reporting of Uncertainty Due to Discretization in CFD Applications. *Journal of Fluids Engineering*, 130(7):078001, 2008.
- [2] ANSYS Inc. *ANSYS CFX-Pre User's Guide, Release 12.0*. Canonsburg, PA, USA, 2009.
- [3] ANSYS Inc. *ANSYS CFX-Solver Theory Guide, Release 12.1*. Canonsburg, PA, USA, 2009.
- [4] G. Boudier, L. Y. M. Gicquel, and T. J. Poinso. Effects of mesh resolution on large eddy simulation of reacting flows in complex geometry combustors. *Combustion and Flame*, 155(1-2):196–214, 2008.
- [5] L. Cunha Caldeira Mesquita. Mesh adaptation for large eddy simulation of combustion chambers flow. Master's thesis, École nationale supérieure de techniques avancées, 2015.
- [6] J. Deeken, D. Suslov, O. Haidn, and S. Schleichriem. Combustion efficiency of a porous injector during throttling of a LOx/H<sub>2</sub> combustion chamber. In *Progress in Propulsion Physics*, pages 251–264, Les Ulis, France, oct 2011. EDP Sciences.
- [7] J. Deeken, D. Suslov, O. Haidn, and S. Schleichriem. Combustion efficiency sensitivity studies of the API injector concept. In *49th AIAA Aerospace Sciences Meeting including the New Horizons Forum and Aerospace Exposition*, Reston, Virginia, jan 2011. American Institute of Aeronautics and Astronautics.
- [8] P. J. Frey and F. Alauzet. Anisotropic mesh adaptation for CFD computations. *Computer Methods in Applied Mechanics and Engineering*, 194(48-49):5068–5082, 2005.
- [9] W. Habashi, J. Dompierre, Y. Bourgault, D. Ait-Ali-Yahia, M. Fortin, and M. G. Vallet. Anisotropic mesh adaptation: towards user-independent, mesh-independent and solver independent CFD. Part I: general principles. *Int. J. Numer. Meth. Fluids*, 32(6):725–744, 2000.
- [10] P. Haldenwang and D. Pignol. Dynamically adapted mesh refinement for combustion front tracking. *Computers and Fluids*, 31(4-7):589–606, 2002.
- [11] V. Hannemann. Numerische Simulation von Stoß-Stoß-Wechselwirkungen unter Berücksichtigung von chemischen und thermischen Nichtgleichgewichtseffekten. Technical report, 1997.

- [12] E. A. Ibrahim, J. R. Kenny, and N. B. Walker. Atomization of Shear Coaxial Liquid Jets. *Applied Physics Research*, 2(1), 2010.
- [13] B. Ivancic and W. Mayer. Time- and Length Scales of Combustion in Liquid Rocket Thrust Chambers. *Journal of Propulsion and Power*, 18(2):247–253, 2002.
- [14] J. D. A. Jr. *Computational Fluid Dynamics - The Basics with Applications*. McGraw-Hill, Inc., 1995.
- [15] S. Karl. Numerical investigation of a generic scramjet configuration. Dissertation, Fakultät Maschinenwesen der Technischen Universität Dresden, 2011.
- [16] J. Lux, D. Suslov, and O. Haidn. On porous liquid propellant rocket engine injectors. *Aerospace Science and Technology*, 12(6):469–477, 2008.
- [17] A. Mack and V. Hannemann. Validation of the unstructured DLR-TAU-Code for hypersonic flows. In *32nd AIAA Fluid Dynamics Conference, St. Louis (USA), 24.-27.06.2002*, 2002.
- [18] B. J. McBride and S. Gordon. Computer Program for Calculation of Complex Chemical Equilibrium Compositions and Applications: II-User Manual and Program Description. *NASA Reference Publication 1311*, 1996.
- [19] C. Roth, O. Haidn, H. Riedmann, B. Ivancic, D. Maestro, B. Cuenot, L. Selle, Y. Daimon, A. Chemnitz, R. Keller, J. Zips, G. Frank, and H. Müller. Comparison of different modeling approaches for CFD simulations of a single-element GCH<sub>4</sub>/GOX rocket combustor. *Sonderforschungsbereich/Transregio 40 – Summer Program Report 2015*, pages 101–118, 2015.
- [20] C. Roth, S. Silvestri, N. Perakis, and O. Haidn. Experimental and Numerical Investigation of Flow and Combustion in a Single Element Rocket Combustor using GH<sub>2</sub>/GOX and GCH<sub>4</sub>/GOX as Propellants. *31st International Symposium on Space Technology and Science*, jun 2017.
- [21] D. Schneider, C. Génin, S. Karl, and V. Hannemann. A numerical model for nozzle flow application under lox/ch<sub>4</sub> hot flow conditions. In *52nd AIAA/SAE/ASEE Joint Propulsion Conference*, jul 2016.
- [22] V. P. Zhukov. Computational Fluid Dynamics Simulations of a GO<sub>2</sub>/GH<sub>2</sub> Single Element Combustor. *Journal of Propulsion and Power*, 31(6):1707–1714, nov 2015.
- [23] V. P. Zhukov and K. P. Heinrich. A Grid Convergence Study for Computational Fluid Dynamic Simulations of Separate Injectors of a Porous Injector Head. In *7th European Conference for Aeronautics and Aerospace Sciences (EUCASS)*, 2017.
- [24] V. P. Zhukov and D. I. Suslov. Measurements and modelling of wall heat fluxes in rocket combustion chamber with porous injector head. *Aerospace Science and Technology*, 48:67–74, jan 2016.

- [25] V. P. Zhukov, D. I. Suslov, and O. J. Haidn. CFD simulation of flow in combustion chamber with porous injector head and transpirationally cooled walls. *4th European Conference for Aerospace Sciences*, 2011. paper ID: 29.